

Chapter 1. Introduction

Vertical-cavity surface-emitting lasers (VCSELs) are well-established devices for applications in optical communications, optical interconnects, optical neural networks, laser printers, high density optical disks, and optical signal processing. Their advantages over edge emitting lasers are longitudinal single mode emission, low threshold current, low divergence circular laser beam, wafer-level testing, and the capability of fabricating dense two-dimensional arrays. A recent innovation is to exploit the selective wet oxidation of the high Al-containing layers within a semiconductor distributed Bragg reflector (DBR) to form one or more buried oxide aperture(s). The selective wet oxidation as a means of current constriction and optical confinement has dramatically enhanced the performance of VCSELs. The benefits of oxide confinement are manifest in properties ranging from low laser threshold and decreased intensity noise to high differential quantum efficiencies and increased modulation bandwidth as compared to other confinement methods such as proton implantation. The oxide-confined VCSEL has many attractive features but also drawbacks stemming from the vertical cavity geometry. For a very short cavity with lateral mode dimensions on the order of tens of wavelengths, a rich variety of mode dynamics can therefore be expected in oxide-confined VCSEL such as the whispering gallery modes [1,2], Hermite-Gaussian, Laguerre-Gaussian modes [3-7], and others [8-10]. Therefore the transverse modal behaviour of the oxide-confined VCSEL is an interesting subject of

laser physics.

To understand the transverse modal behaviour, we experimentally investigate the round aperture oxide-confined VCSELs with diameter of the 20 μm oxide aperture. Due to the high quality of the processed wafer, the near- and far-field images and corresponding spectrum are measured for a wide range of injection currents even well above the thermal roll-over point. The complex flower-like and y-junction structured transverse mode patterns are observed in far-field images of broad-area oxide-confined VCSELs. To identify the influence of the guiding mechanisms on the transverse modal behaviour, we compare the experimental data of 20 μm diameter oxide-confined VCSEL to proton-implanted VCSEL. We find that the inhomogeneous carrier distribution which is more pronounced in the broad-area devices, dominate the properties of transverse mode. At high pump rates, the influence of thermal gradient inside the cavity becomes stronger which leads to a further preference of high order modes. Furthermore, the transverse modal behaviour of VCSELs depends strongly on the confinement mechanism which is demonstrated on boundary effect caused by oxide layers. The emission of multi-high-order mode is a consequence of the combination of these effects, and thus lead the formation of complex flower-like and y-junction structured transverse mode patterns.

The dissertation is organized as follows: the manufacturing of the

oxide-confined VCSELs and experimental setup are presented in chapter 2. In chapter 3, we show the experimental results of oxide-confined VCSELs with various aperture diameters. Furthermore, the experimental result of oxide-confined VCSEL is compared with the proton-implanted VCSEL (20 μm in diameter). We present the numerical simulation for the formation of the y-junction structured pattern in chapter 4. The different contributions to the transverse modal behaviour are then discussed and the results of this dissertation are summarized in the chapter 5.

References

- [1] H. Deng, Q. Deng, and D. G. Deppe, “Native-oxide laterally confined whispering-gallery mode laser with vertical emission”, Appl. Phys. Lett., 69, pp. 3120-3122, 1996.
- [2] Q. Deng, H. Deng, and D. G. Deppe, “Radiation fields from whispering-gallery modes of oxide-confined vertical-cavity surface-emitting lasers”, Opt. Lett., 22, pp. 463-465, 1997.
- [3] C. Degen, I. Fischer, and W. Elsasser, “Transverse modes in oxide confined VCSELs: influence of pump profile, spatial hole burning, and thermal effects”, Opt. Exp., 5, pp. 38-47, 1999.
- [4] C. Degen, B. Krauskopf, G. Jennemann, I. Fischer, and W. Elsasser, “Polarization selective symmetry breaking in the near-fields of vertical cavity surface emitting lasers” J. Opt. B: Quantum & Semiclassical Opt., 2, pp. 517-525, 2000.
- [5] C. Degen, I. Fischer, W. Elsasser, L. Fratta, P. Debernardi, G. P. Bava, M. Brunner, R. Hovel, M. Moser, and K. Gulden, “Transverse modes in thermally detuned oxide-confined vertical-cavity surface-emitting lasers”, Phy. Rev. A, 63, pp. 023817/1-023817/12, 2001.
- [6] P. Debernardi, G. P. Bava, C. Degen, I. Fischer, and W. Elsasser, “Influence of anisotropies on transverse modes in oxide-confined VCSELs”, IEEE J. Quantum Electron., 38, pp. 73-84, 2002.
- [7] D. L. Huffaker, H. Deng, Q. Deng, and D. G. Deppe, “Ring and stripe oxide-confined vertical-cavity surface-emitting lasers”, Appl. Phys.

- Lett., 69, pp. 3477-3479, 1996.
- [8] S. P. Hegarty, G. Huyet, J. G. McInerney, and K. D. Choquette, “Pattern formation in the transverse section of a laser with a large Fresnel number”, Phys. Rev. Lett., 82, pp. 1434-1437, 1999.
- [9] S. P. Hegarty, G. Huyet, P. Porta, J. G. McInerney, K. D. Choquette, K. M. Geib, and H. Q. Hou, “Transverse-mode structure and pattern formation in oxide-confined vertical-cavity semiconductor lasers”, J. Opt. Soc. Am. B, 16, pp. 2060-2071, 1999.
- [10] T. Ackemann, S. Barland, M. Cara, S. Balle, J. R. Tredicce, R. Jager, M. Grabherr, M. Miller, and K. J. Ebeling, “Spatial mode structure of bottom-emitting broad-area vertical-cavity surface-emitting lasers”, J. Opt. B: Quantum & Semiclassical Opt., 2, pp. 406-412, 2000.

Chapter 2. Experiment

2.1 Introduction

The performance characteristics of VCSELs are strongly influenced by the epitaxial structure and fabrication processes that are employed. For example, one focus of VCSEL development has been toward reduced threshold current; therefore, processing technology producing laser structures designed for enhanced transverse confinement have had significant impact. A recent innovation is to provide lateral material variation surrounding a semiconductor laser diode through the selective wet oxidation of buried AlGaAs layers [1-4]. Exposing AlGaAs alloys to temperatures from 350 to 500 °C in a steam environment converts the semiconductor into a mechanically robust, chemically inert, insulating, and low refractive index oxide [5]. Wet oxidation of AlGaAs has been successfully employed in the fabrication of edge-emitting lasers [6-8] and recently been applied to VCSEL fabrication. Oxide layers converted from AlAs or AlGaAs have been incorporated into hybrid VCSELs, which use a dielectric top DBR mirror [9], and into monolithic VCSELs, which use a semiconductor top DBR mirror [10]. The oxide layers within selectively oxidized VCSELs effectively confine both electrons and photons and thus serve to define the transverse optical cavity.

The fabrication of oxide-confined VCSEL structure, the requisite

processing technologies and experimental setup used to investigate the transverse modal behavior of the laser are described in this chapter. The fabrication of oxide-confined VCSEL is presented in Section 2.2. In Section 2.3 the structure of the oxide-confined VCSEL under investigation is briefly described. The experimental setup used to investigate the transverse modal behavior of the laser is considered in Section 2.4.

2.2 Fabrication of Oxide-Confined VCSEL

2.2.1 Processing of Oxide-Confined VCSEL

Fabrication of selectively oxidized monolithic VCSELs is predicated on designing the layer compositions, and thus the oxidation rate, such that specific oxide layers near the laser cavity have a greater lateral extent to define an oxide aperture, as depicted in Fig. 2-1 [10,11]. The oxidation selectivity to Al composition is exploited to fabricate the buried oxide layers within a VCSEL: With minute changes of Ga concentration, one or more AlGaAs layers are induced to oxidize more rapidly and thus form buried oxide layers for electrical and optical confinement. The selectively oxidized VCSELs described in the following are grown by metal-organic chemical vapor deposition (MOCVD), which has the advantages of accessibility of the complete AlGaAs alloy range, and stringent compositional uniformity and control. The rapid growth rate, high wafer throughput, run-to-run stability, wafer uniformity, and broad flexibility of available materials make MOCVD an appropriate VCSEL manufacturing

platform.

The processing steps for the oxidized VCSEL are presented in Fig. 2-2. Fabrication of selectively oxidized VCSELs begins with the deposition of electrical contacts. A silicon nitride mask is deposited and patterned on the wafer top to encapsulate the metal contact and to form an etch mask. Dry etching, such as reactive ion etching, is used to define mesas or holes to expose the oxidation layers. For mesa structures [11], the oxide aperture is formed by oxide layer(s) extending from the edge into the center of the mesa. For etched hole planar structures [12], the aperture is formed by the overlap of oxides that extend outward from each hole. The lateral oxidation extent of a layer within the etched mesa or surrounding the etched hole is controlled by the composition of the layer and the oxidation time. Typically, an oxidation temperature of 440 produces an oxidation rate of approximately 1 $\mu\text{m}/\text{min}$ for the $\text{Al}_{0.98}\text{Ga}_{0.02}\text{As}$ layers [10]. After oxidation the nitride mask is removed to permit laser testing.

For a given oxidation time and thus lateral extent of oxidation, variation of the oxide aperture area within a sample can be obtained using different mesa sizes or separation between the etched holes. For mesa-etched oxide structures, planarization can be accomplished using polyimide as a backfill, or an air bridge technology can be used to allow deposition of metal interconnects. A planar VCSEL configuration conducive to the deposition of bonding pads results using the etched-hole

oxide structures, but electrical isolation between VCSELs must still be accomplished by some technique such as stacked ion implantation.

2.2.2 Apparatus and Method of Selective Wet Oxidation

The wet oxidation of AlGaAs is a relatively simple procedure: expose high Al-content layers to water vapor transported in an inert gas within an elevated temperature (350-500 °C) environment [5]. However, establishing a stable and reproducible oxidation process requires careful control of several process parameters [13]. In Fig. 2-3, we show an oxidation system which incorporates mass flow controllers, a stable water vapor source, and a three-zone 4 inch diameter tube furnace. The system is supplied by bubbling N₂ or other inert gas through deionized water, which in turn is immersed within a constant-temperature bath maintained at 90 °C. The gas passes through the bubbler and into a three-zone furnace through a heated tube to avoid condensation. The stringent control of gas flow, bubbler water temperature, and furnace temperature enables a stable and reproducible oxidation process.

Monolithic selectively oxidized VCSEL typically contains multilayers of high and low Al-containing AlGaAs alloys [10]. For lateral oxidation of buried layers, mesas or holes are isotropically etched to expose the layers immediately before oxidation, although delays (e.g. several days) between etching and oxidation of AlGaAs do not significantly influence the oxidation rates. The oxidation system in Fig. 2-4 is allowed to equilibrate

with carrier gas and steam flowing before each oxidation run. The oxidation samples are placed on a preheated platen which is inserted into the furnace. The composition of the epitaxial layers vary such that one or more buried layers will oxidize laterally within the mesa to a greater extent than the surrounding layers as depicted in Fig. 2-1. The oxidation extent is controlled by the time of oxidation. The refractive index difference between the oxidized and unoxidized region within the sample makes the oxide/semiconductor interface within the mesa apparent under visible or infra-red illumination. This allows measurement of the oxidation extent and rate, and can be used to identify the oxide aperture within the VCSEL.

2.2.3 Oxidation Rate Dependencies

To develop a manufacturable wet oxidation technique, the influences of process parameters such gas flow, gas composition, temperature, Al composition and layer thickness on the rate of oxidation have been characterized [14]. The oxidation dependencies will dictate the degree of control of these parameters required in an oxidation system, as well as the compositional control and uniformity required in the epitaxial structures, to achieve a reproducible oxidation fabrication technology.

The lateral oxidation has a temperature-dependent linear oxidation rate without an induction time preceding the onset of oxidation [17,18]. Using a simple oxidation model [19], the oxidation thickness, d_{ox} , achieve in a time t is:

$$d_{ox}^2 + A d_{ox} = B t \quad (2-1)$$

where B is related to the diffusion constant of the reactants moving through the oxidation and B/A is related to the oxidation reaction rate constant and/or the rate of reactant supply at the oxide boundary. In the limit of short oxidation times and/or thin oxide thickness, Equation (2-1) yields linear growth:

$$d_{ox} = (B/A)t \quad (2-2)$$

For greater oxidation lengths or higher temperatures, parabolic growth rate may arise [20,21]. We observe a lack of an induction time before oxidation, even for samples that are pre-etched and exposed to the atmosphere prior to oxidation.

A high degree of oxidation selectivity between AlGaAs layers can thus be obtained with only a small change in Al concentration. It is this oxidation selectivity which can be exploited for the fabrication of buried oxide layers within a VCSEL: with minute changes of Ga concentration, specific or multiple AlGaAs layer(s) can be selected out to form buried oxide layers for electrical and optical confinement (see Fig. 2-1).

The thickness of the semiconductor layer to be oxidized can also influence its oxidation rate [22,23]. It is obvious that the oxidation rate dependence on thickness can compensate for the compositional dependence:

thin layers of AlAs may oxidize slower than thick layers of AlGaAs. Note that linear oxidation rates are still observed during oxidation of thin layers, indicating that decreased reactant transport through a thin layer is not responsible for the reduced oxidation rate. Variations of the surface energy at the oxide terminus [23] or changes of strain with thickness will influence the oxidation rate.

Finally, the composition of the surrounding layers will affect the oxidation rate [24,25] and shape of the oxide terminus [26] through diffusion and supply of reactants. For example, the thickness of a GaAs barrier between $\text{Al}_{0.98}\text{Ga}_{0.02}\text{As}$ and $\text{Al}_{0.94}\text{Ga}_{0.06}\text{As}$ layers has been shown to influence the oxidation rate of the latter by mediating the vertical diffusion of reactants [25]. A rapidly oxidizing layer can supply reactants to its surrounding layers such that significant vertical oxidation into the adjoining layers occurs. The vertical oxidation can lead to an enhanced effective lateral oxidation rate as well as a tapered profile at the oxidation terminus. Finally, by carefully tailoring the Al-content along the epitaxial growth direction, a vertical oxidation profile from a planar oxidized film has been demonstrated [27]. Therefore, in order to accurately predict the oxidation rate and profile of buried layers of AlGaAs, the composition and thickness of the semiconductor layer intended for oxidation and the surrounding layers must all be taken into account.

2.3 Structure of Oxide-Confined VCSELs

The oxide-confined VCSELs under investigation are grown on a GaAs substrate using MOCVD to operate at approximately 809 nm. The active region consists of three $\text{Al}_{0.08}\text{Ga}_{0.92}\text{As}$ - $\text{Al}_{0.36}\text{Ga}_{0.64}\text{As}$ quantum wells, which are embedded in the spacer layers to form the cavity with a thickness of one-wavelength. The Bragg mirrors consist of AlGaAs $\lambda/4$ layers with different aluminum content and graded interfaces in terms of material composition. The confinement of both the carriers and the optical field is achieved by means of a high-Al composition $\text{Al}_{0.97}\text{Ga}_{0.03}\text{As}$ layer in the first top-mirror layer with a central window of unoxidized material. The wafers are wet oxidized at 425 °C and the oxidation time is controlled to fabricate the oxide aperture with 20 μm diameter in a 110 μm in diameter mesa structure. Then a SiN passivation layer is deposited followed by Ti-AuBe-Au P-metal evaporation. The AuGe-Au N-metal is finally evaporated and annealed after thinning the substrate thickness to 200 μm .

2.4 Experimental Setup

We record images of the intensity distributions of the lasing near- and far-field and corresponding spectrum data of the VCSELs during lasing operation in order to obtain information about the transverse mode structure. The experimental setups for the recording of the near- and far-field images are shown in Fig. 2-4. We couple the near-field image onto the beam profiler using a collimating objective lens. As for far-field image, we project the far-field pattern on a screen and then record it with a CCD

camera (Coherent, Beam-Code). An optical spectrum analyzer (ADVANTEST Q8347) is used to monitor the spectral information of the laser.

References

- [1] C. W. Wilmsen, H. Temkin, and L. A. Coldren, Vertical-cavity surface-emitting lasers: design, fabrication, characterization, and applications, Cambridge university press, New York, 1999.
- [2] J. Cheng, and N. K. Dutta, Vertical-cavity surface-emitting lasers: technology and applications, Gordon & Breach, Amsterdam, 2000.
- [3] W. T. Tsang, “Self-terminating thermal oxidation of AlAs epilayers grown on GaAs by molecular beam epitaxy”, Appl. Phys. Lett., 33, pp. 426-429, 1978.
- [4] J. M. Dallesasse, N. Holonyak, Jr., A. R. Sugg, T. A. Richard, and N. El-Zein, “Hydrolyzation oxidation of $\text{Al}_x\text{Ga}_{1-x}\text{As-AlAs-GaAs}$ quantum well heterostructures and superlattices”, Appl. Phys. Lett., 57, pp. 2844-2846, 1990.
- [5] N. Holonyak, Jr., and J. M. Dallesasse, USA Patent #5, 262, 360, 1993.
- [6] J. M. Dallesasse and N. Holonyak, Jr., “Native-oxide stripe-geometry $\text{Al}_x\text{Ga}_{1-x}\text{As-GaAs}$ quantum well heterostructure lasers”, Appl. Phys. Lett., 58, pp. 394-396, 1991.
- [7] F. A. Kish, S. J. Caracci, N. Holonyak, Jr., J. M. Dallesasse, K. C. Hsieh, M. J. Ries, S. C. Smith, and R. D. Burnham, “Planar native-oxide index-guided $\text{Al}_x\text{Ga}_{1-x}\text{As-GaAs}$ quantum well heterostructure lasers”, Appl. Phys. Lett., 59, pp. 1755-1757, 1991.
- [8] S. A. Maranowski, F. A. Kish, S. J. Caracci, N. Holonyak, Jr., J. M. Dallesasse, D. P. Bour, and D. W. Treat, “Native-oxide defined

- $\text{In}_{0.5}(\text{Al}_x\text{Ga}_{1-x})_{0.5}\text{P}$ quantum well heterostructure window lasers (660 nm)”, Appl. Phys. Lett., 61, pp. 1688-1690, 1992.
- [9] D. L. Huffaker, D. G. Deppe, K. Kumar, and T. J. Rogers, “Native-oxide defined ring contact for low threshold vertical-cavity lasers”, Appl. Phys. Lett., 65, pp. 97-99, 1994.
- [10] K. D. Choquette, R. P. Schneider, Jr., K. L. Lear, and K. M. Geib, “Low threshold voltage vertical-cavity lasers fabricated by selective oxidation”, Electron. Lett., 30, pp. 2043-2044, 1994.
- [11] K. D. Choquette, K. L. Lear, R. P. Schneider, Jr., K. M. Geib, J. J. Figiel, and R. Hull, “Fabrication and performance of selectively oxidized vertical-cavity lasers”, IEEE Photon. Tech. Lett., 7, pp. 1237-1239, 1995.
- [12] C. L. Chua, R. L. Thornton, and D. W. Treat, “Planar laterally oxidized vertical-cavity lasers for low threshold high density top surface emitting arrays”, IEEE Photon. Tech. Lett., 9, pp. 1060-1061, 1997.
- [13] K. M. Geib, K. D. Choquette, H. Q. Hou, and B. E. Hammons, “Fabrication issues of oxide-confined VCSELs”, in Vertical-Cavity Surface-Emitting Lasers, edited by K. D. Choquette and D. G. Deppe, SPIE, 3003, pp. 69-74, 1997.
- [14] K. D. Choquette, K. M. Geib, C. I. H. Ashby, R. D. Twisten, O. Blum, H. Q. Hou, D. M. Follstaedt, B. E. Hammons, D. Mathes, and R. Hull, “Advances in selective oxidation of AlGaAs alloys”, J. Special Topics of Quantum Electron., 3, pp. 916-926, 1997.
- [15] C. I. H. Ashby, J. P. Sullivan, K. D. Choquette, K. M. Geib, and H. Q.

- Hou, "Wet oxidation of AlGaAs: the role of hydrogen", J. Appl. Phys., 82, pp. 3134-3136, 1997.
- [16] K. D. Choquette, K. M. Geib, H. C. Chui, H. Q. Hou, and R. Hull, "Selective oxidation of buried AlGaAs for fabrication of vertical-cavity lasers", Mat. Res. Soc. Symp. Proc., 421, pp. 53-61, 1996.
- [17] R. S. Burton and T. E. Schlesinger, "Wet thermal oxidation of $\text{Al}_x\text{Ga}_{1-x}\text{As}$ compounds", J. Appl. Phys., 76, pp. 5503-5507, 1994.
- [18] H. Nickel, "A detailed experimental study of the wet oxidation kinetics of $\text{Al}_x\text{Ga}_{1-x}\text{As}$ layers", J. Appl. Phys., 78, pp. 5201-5203, 1995.
- [19] D. E. Deal and A. S. Grove, "General relationship for the oxidation of silicon", J. Appl. Phys., 36, pp. 3770, 1965.
- [20] F. A. Kish, S. A. Maranowski, G. E. Hofler, N. Holonyak, Jr., S. J. Caracci, J. M. Dallesasse, and K. C. Hsieh, "Dependence on doping type (p/n) of the water vapor oxidation of the high-gap $\text{Al}_x\text{Ga}_{1-x}\text{As}$ ", Appl. Phys. Lett., 60, pp. 3165-3167, 1992.
- [21] M. Ochiai, G. E. Giudice, H. Temkin, J. W. Scott, and T. M. Cockerill, "Kinetics of thermal oxidation of AlAs in water vapor", App. Phys. Lett., 68, pp. 1898-1900, 1996.
- [22] J. H. Kim, D. H. Lim, K. S. Kim, G. M. Yang, K. Y. Lim, and H. J. Lee, "Lateral wet oxidation of $\text{Al}_x\text{Ga}_{1-x}\text{As}$ -GaAs depending on its structure", Appl. Phys. Lett., 69, pp. 3357, 1996.
- [23] R. L. Naone and L. A. Coldren, "Surface energy model for the thickness dependence of the lateral oxidation of AlAs", J. Appl. Phys., 82, pp. 2277-2280, 1997.

- [24] M. H. MacDougal, P. D. Dapkus, A. E. Bond, C. K. Lin, and J. Geske, “Design and fabrication of VCSELs with Al_xO_y-GaAs DBRs”, J. Special Topics of Quantum Electron., 3, pp. 905-915, 1997.
- [25] O. B. Blum and C. I. H. Ashby, “Barrier-layer-thickness control of selective wet oxidation of AlGaAs for embedded optical elements”, Appl. Phys. Lett., 70, pp. 2870-2872, 1996.
- [26] R. L. Naone, E. R. Hegbloom, B. J. Thibeault, and L. A. Coldren, “Oxidation of AlGaAs layers for tapered apertures in vertical cavity lasers”, Electron. Lett., 33, pp. 300, 1997.
- [27] P. W. Evans and N. Holonyak, “Planar anisotropic oxidation of graded AlGaAs for high resolution vertical-wall current and light guiding in laser diodes”, Appl. Phys. Lett., 71, pp. 261-263, 1997.
- [28] K. D. Choquette and H. Q. Hou, “Vertical-cavity surface-emitting lasers: moving from research and manufacturing”, Proceedings of IEEE, 85, pp. 1730-1739, 1997.
- [29] S. P. Hegarty, G. Huyet, P. Porta, J. G. McInerney, K. D. Choquette, K. M. Geib, and H. Q. Hou, “Transverse-mode structure and pattern formation in oxide-confined vertical-cavity semiconductor lasers”, J. Opt. Soc. Am. B, 16, pp. 2060-2071, 1999.

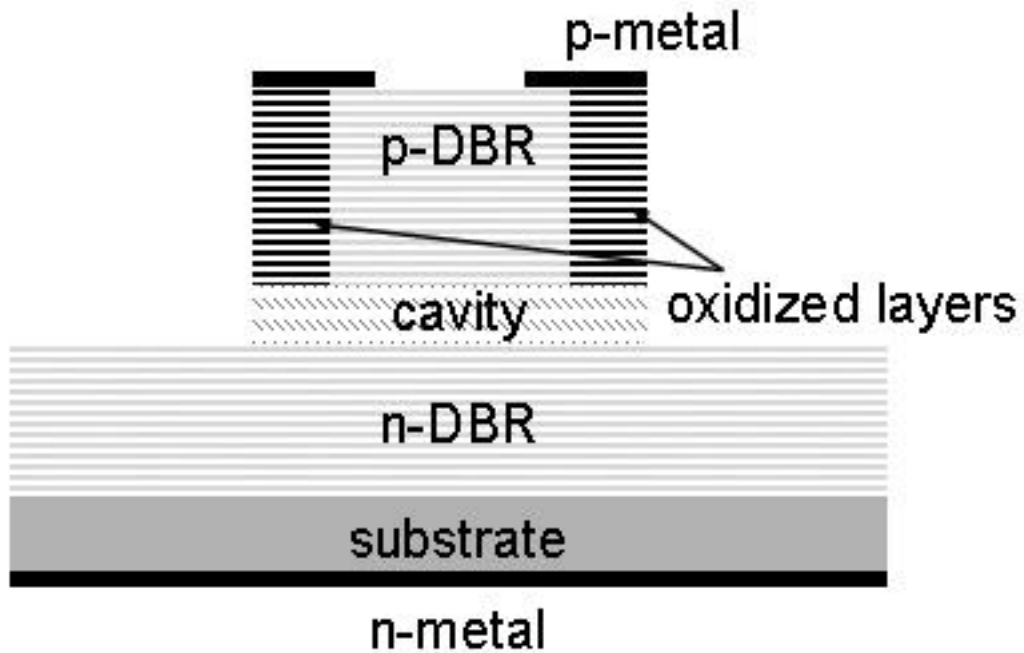


Fig. 2-1 Cross-section sketch of a selectively oxidized VCSEL composed of GaAs/AlGaAs multilayers and buried oxide layers. The highest Al-containing layers on each side of the optical cavity extend further into the mesa than the other oxidized layers, forming an oxide aperture at the mesa center.

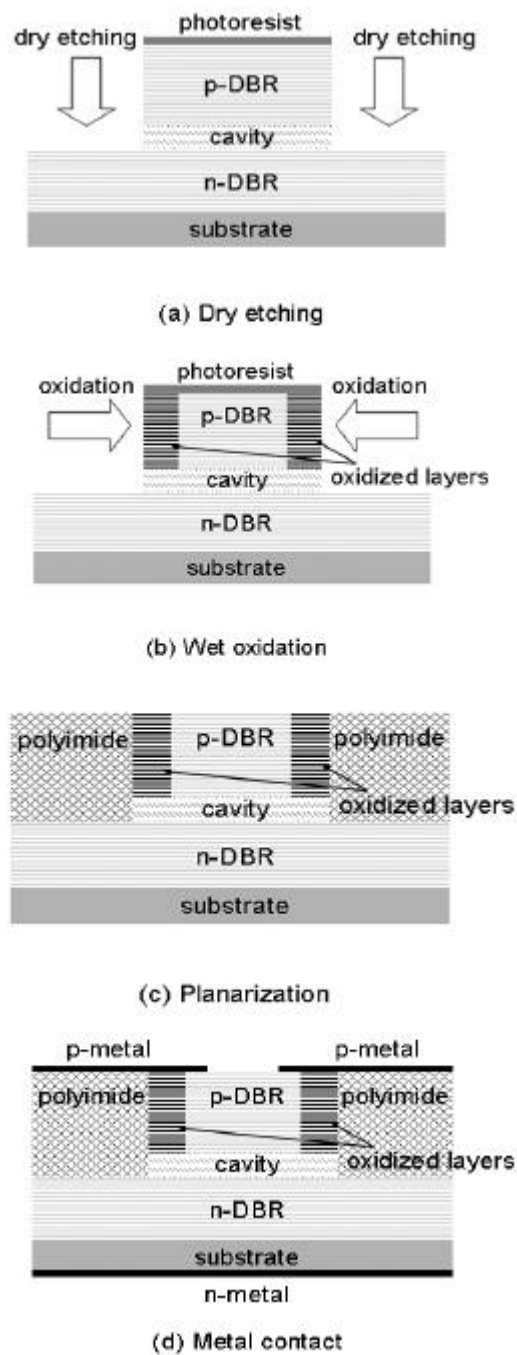


Fig. 2-2 Graphic presentation of the processing steps for the oxidized VCSEL.

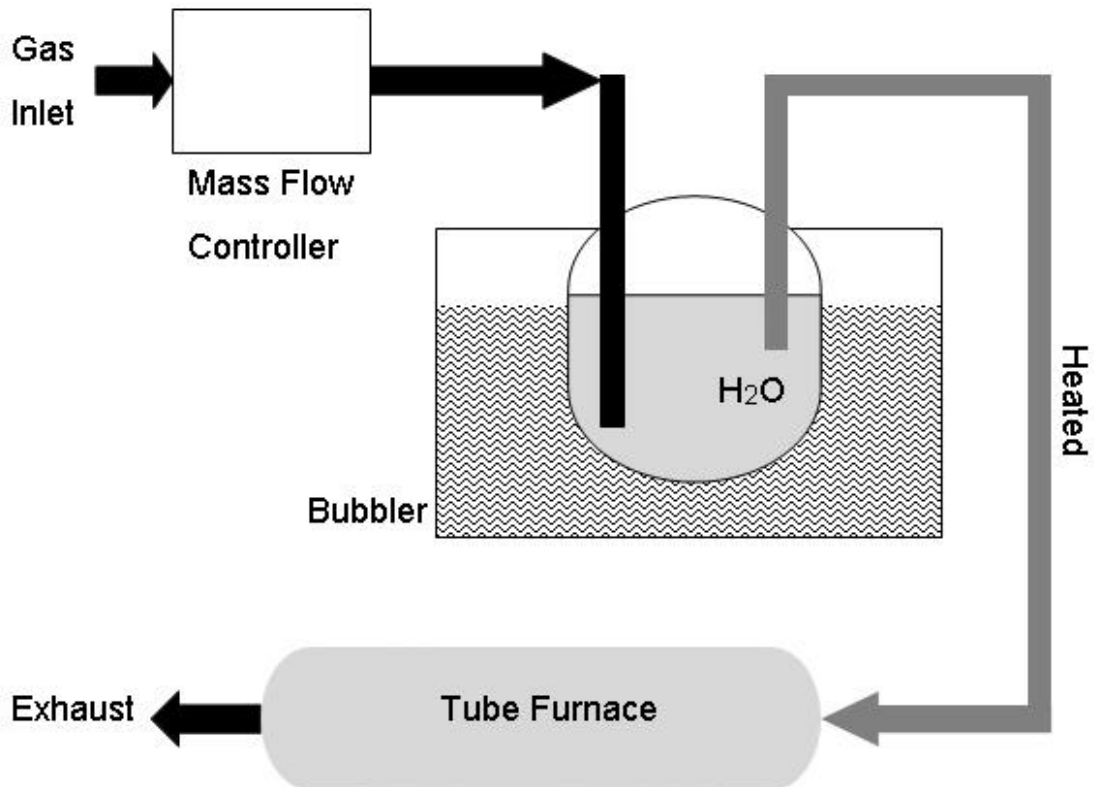


Fig. 2-3 Apparatus for the reproducible wet oxidation of AlGaAs alloys which employs mass flow gas controllers, a constant temperature water bubbler, and a three zone furnace [2].

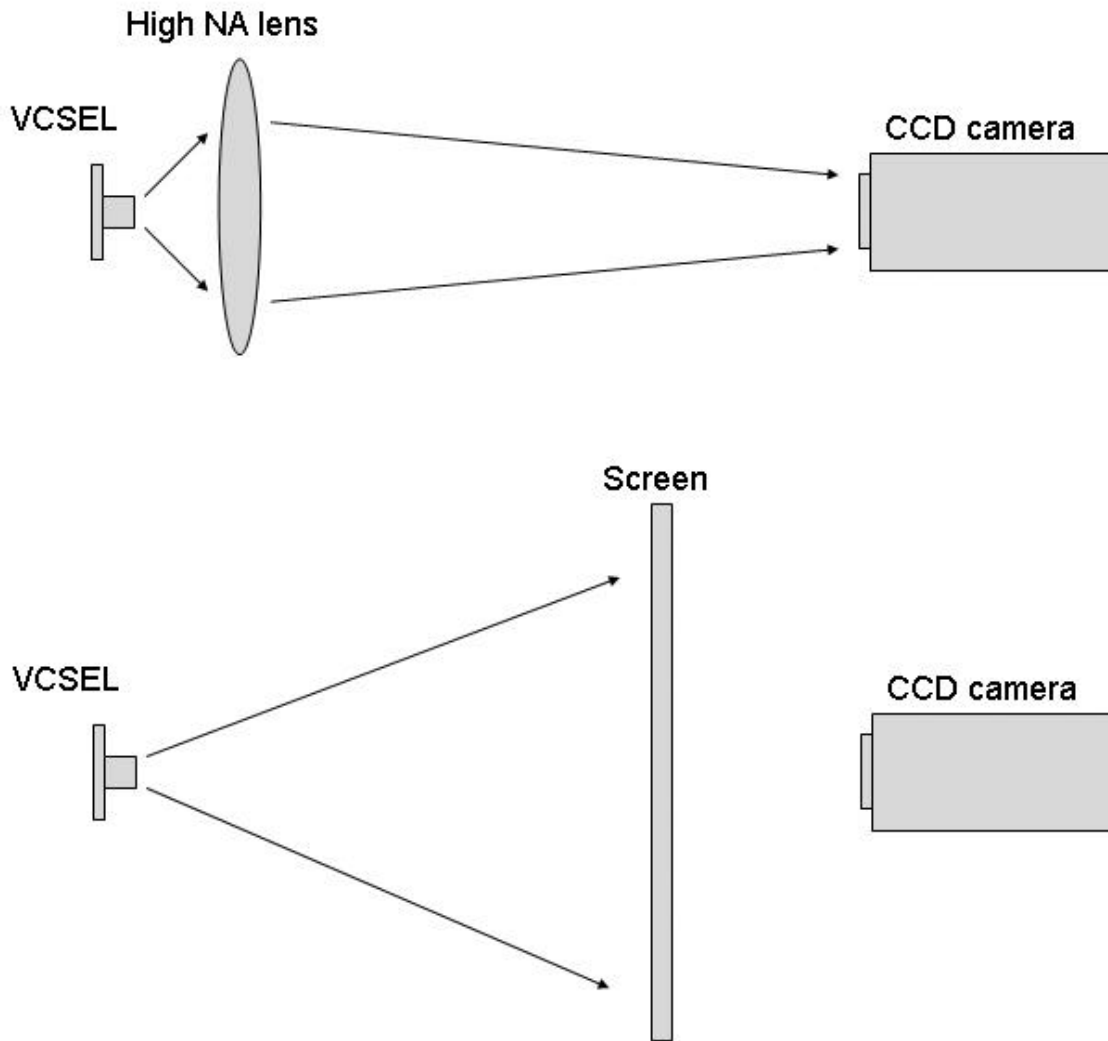


Fig. 2-4 Methods used to obtain near-field (top) and far-field (bottom) intensity distributions. A lens of high numerical aperture was used to focus the highly divergent emission onto a distant CCD array to obtain a magnified image. For the far-field, a piece of paper was mounted to act as a diffusion screen, and the scattered light imaged by a CCD camera [29].

Chapter 3. Experimental Results

3.1 Introduction

We present experimental data characterizing the transverse modes in a broad-area (20 μm in diameter) oxide-confined vertical-cavity surface-emitting laser under CW operation at room temperature. The optical power versus injection current characteristic, near- and far-fields images are presented in section 3.2. In section 3.3, we show the structure information and experimental results of the proton-implanted VCSEL, which are compared with the experimental data of the oxide-confined VCSEL.

3.2 20 μm Aperture Diameter Oxide-Confined VCSEL

The optical power versus injection current characteristic of 20 μm aperture diameter oxide-confined VCSEL is shown in Fig. 3-1, which reveals significant thermal roll-over behavior. Its threshold current is ~ 2.7 mA and its maximum power is ~ 6.4 mW.

Near-field images of the 20 μm diameter oxide-confined VCSEL are presented in Fig. 3-2 which contains images for injection currents 10.5 mA (a), 13.4 mA (b), 20.0 mA (c), 22.3 mA (d), 23.0 mA (e) and 23.3 mA (f). A noncircular symmetry of the transverse mode can be already seen from a

first look at the optical near-field images because of the anisotropic oxidation speed [1]. The high-intensity distribution can only be observed around the periphery of the oxide aperture as shown in Fig. 3-2(a) ~ (e). These results indicate that the multiple high-order transverse modes tend to gather around the periphery of the oxide aperture due to a strong optical confinement induced by the oxidized layers. Therefore the detail structure of transverse mode pattern cannot be observed in the near-field images. At an even larger injection current of 23.3 mA, the lasing near-field pattern becomes a pure single high-order mode which has 18 spots as shown in Figs. 3-2(f). The results reveal that the mode suppression is strongly influenced by thermal effect, and the inhomogeneous distributions of spatial carriers and thermal gradients in the laser cause a strong tendency towards the emission of high-order transverse modes [2].

We present the far-field intensity distribution in Fig. 3-3, which contains the 180°-rotation symmetrical images at injection currents of 10.5 mA (a), 13.4 mA (b), 20.0 mA (c), 22.3 mA (d), 23.0 mA (e) and 23.3 mA (f). The far-field image shows a doughnut-liked pattern at injection current of 10.5 mA. At higher injection current of 13.4 mA, some radial structures appear at the periphery of doughnut-liked pattern, which is illustrated in Fig. 3-3(b) ~ (c). The y-junction structured pattern is observed in Fig. 3-3(d) ~ (e) and a 9th-order daisy mode is observed in Fig. 3-3(f). Since the lasing modes of the VCSEL at 22.3 mA are multiple transverse modes and these high-order transverse modes have similar divergent angles in far-field

emission as shown in Fig. 3-3(d) ~ (e), we conclude that the interaction between the adjacent high-order transverse modes induces the formation of the y-junction structured pattern.

3.3 Comparison between Oxidized and Implanted VCSEL

3.3.1 Structure of Proton-Implanted VCSEL

VCSEL fabrication generally involves establishing electrical contact to the anode and cathode of the diode and defining the transverse extent of the optical cavity. For the latter, a means of confinement for photons and/or electrons must be implemented. A method to achieve electrical confinement in a planar VCSEL topology is to utilize ion implantation [3-5]. Implantation of ions into the top DBR mirror can be used to render the material around the laser cavity nonconductive and thus to concentrate the injected current into the active medium as depicted in Fig. 3-4. Damage, primarily crystal vacancies created by the implanted ions, compensate the free carriers leading to regions of high resistivity. Hence the ion does is chosen to sufficiently compensate the dopant impurities in the DBR.

The ion implantation energy required to achieve current confinement within a VCSEL depends upon the mass of the ion used and the implant depth desired. Thus the maximum vacancy concentration can be tailored to a specific depth within the DBR mirror. Various ion species have been employed (H^+ , O^+ , N^+ , F^+), although proton implants are the most common.

The peak implant damage is usually designed to occur somewhat above the quantum wells to avoid excessive damage to the active medium [6].

Fabrication of implanted VCSELs will usually begin with the deposition of electrical contacts. It is advantage to deposit the top contact as the first processing step to avoid surface damage (such as unintentional removal of a GaAs cap layer protecting underlying AlGaAs DBR layers) during subsequent steps, which may degrade the ohmic contact. Next an implantation mask of photoresist [5] or plated metal can be used to block the ions and thus define the laser cavity. The simplicity and versatility of photoresist implant masks usually make them more favorable as compared to metal masks. It is also beneficial to have the implant mask extend over the metal contact as depicted in Fig. 3-4 to ensure that electrical contact to an unimplanted region of the VCSEL is maintained [7].

Deep proton implants near the active region are used to define the transverse extent of the laser cavity. As a generic example, a 300 keV proton implant with a dose of $4 \times 10^{14} \text{ cm}^{-3}$ could be employed for an 850 nm VCSEL with a 20-period $\text{Al}_{0.6}\text{Ga}_{0.4}\text{As}/\text{AlAs}$ DBR (2.6 μm thick). A 300 keV proton implant would require a photoresist implant mask thicker than 6 μm . To avoid ion channeling during implantation, the samples are typically inclined by \mathcal{T} from normal. The photoresist mask can be angle etched to match the trajectory of the ion beam [8] and avoid “shadowing” of the ions from the inclined mask, which will produce thin regions of

highly damaged material at shallow depths around the cavity perimeter.

To electrically isolate the VCSEL from neighboring devices, multiple stacked implants with successively decreased energy can be used [4]. Surrounding the periphery of the VCSEL contact in Fig. 3-4 are stacked implanted regions defined by a larger implant mask to fashion a highly resistive region extending from the optical cavity up to the wafer surface. A combination of deep proton and shallow O⁺ implantation is effective to laterally isolate the VCSELs; the latter implant is beneficial for the near surface region because of the high dopant concentration typically present. Finally, an interconnect metal layer can be defined to link the VCSELs with contact pads. Therefore a completely planar VCSEL structure can be implemented with a combination of implantation steps, which is amenable to low cost and high volume manufacture [9].

3.3.2 20 μm Aperture Diameter Proton-Implanted VCSEL

The optical power versus injection current characteristics of proton-implanted VCSELs is shown in Fig. 3-5. The laser has a significant thermal roll-over behavior. The proton-implanted VCSEL has threshold current of ~ 2.4 mA and maximum power of ~ 6.0 mW.

The far-field patterns of proton-implanted VCSELs are shown in Fig. 3-6 which contains images for injection currents 4 mA (a), 17 mA (b), 24 mA (c), 34 mA (d), 41 mA (e) and 59 mA (f). At current of 4.0 mA, the

VCSEL emits in the fundamental transverse mode, which is a Hermite-Gaussian TEM_{00} mode. With increased injection current, the far-field distribution becomes higher order Hermite-Gaussian mode as shown in Fig. 3-6(b) ~ (e). A pure high order Laguerre-Gaussian mode TEM_{011} is present in the far-field image for the injection current of 59.0 mA. At this injection current, the L-I curve of proton-implanted VCSEL has already a negative slope and the optical output power is reduced to only 4.1 mW. Similar to proton-implanted VCSELs in Fig. 3-3(f), the strong heating results in local gain suppression in the center of the laser, which overbalances the confining effect of thermal lensing, and thus favors the formation of high order modes [10].

At low pumping current, the carrier distribution in large-diameter implanted VCSEL is more uniform than in oxidized VCSEL. The smooth and broad pumping profile with a maximum in the center of the implanted VCSEL emits in the fundamental transverse mode, but the high order mode is emitted by carrier profile with pronounced maxima at the periphery and a minimum in the center of the oxidized VCSEL. In Fig. 3-3(a) and 3-6(a), the implanted VCSEL emit in the fundamental transverse mode in contrast to high order mode emitted by the oxidized VCSEL when the pumping current near threshold. From the comparison, we conclude that the inhomogeneous carrier distribution in large diameter oxidized VCSELs is enhanced by strong carrier confinement. The significant carrier confinement supported by oxidized VCSEL makes carrier accumulate at

the periphery, which tends to emit high order mode. With further increasing pumping current, the influence of thermal effect is predominant either in implanted and oxidized VCSELs. The effect of thermal gradients and thermally induced gain suppression become so strong at high injection current, and a ring-shaped carrier distribution arises, which leads to the emission of high order modes.

References

- [1] P. Debernardi, G. P. Bava, C. Degen, I. Fischer and W. Elsasser, “Influence of anisotropies on transverse modes in oxide-confined VCSELs”, IEEE J. Quant. Electron., 38, pp. 73-84, 2002.
- [2] C. Degen, I. Fischer and W. Elsasser, “Transverse modes in oxide confined VCSELs: influence of pump profile, spatial hole burning, and thermal effects”, Opt. Exp., 5, pp. 38-47, 1999.
- [3] K. Tai, R. J. Fischer, K. W. Wang, S. N. G. Chu and A. Y. Cho, “Use of implant isolation for fabrication of vertical-cavity surface-emitting laser diodes”, Electron. Lett., 25, pp. 1644-1645, 1989.
- [4] M. Orenstein, A. V. Lehmen, C. J. Chang-Hasnain, N. G. Stoffel, J. P. Harbison, L. T. Florez, E. Clausen and J. L. Jewell, “Vertical-cavity surface-emitting InGaAs/GaAs lasers with planar lateral definition”, Appl. Phys. Lett., 56, pp. 2384-2386, 1990.
- [5] Y. H. Lee, B. Tell, K. F. Brown-Goebeler and J. L. Jewell, “Top-surface-emitting GaAs four-quantum-well lasers emitting at 0.85 μm ”, Electron. Lett., 26, pp. 710-711, 1990.
- [6] W. Jiang, C. Gaw, P. Kiely, B. Lawrence, M. Lebby and P. R. Claisse, “Effect of proton implantation on the degradation of GaAs/AlGaAs vertical cavity surface emitting lasers”, Electron. Lett., 33, pp. 137-139, 1997.
- [7] G. Hasnain, K. Tai, L. Yang, Y. H. Wang, R. J. Fischer, J. D. Wynn, B.

- Weir, N. K. Dutta and A. Y. Cho, "Performance of gain-guided surface emitting lasers with semiconductor distributed Bragg reflectors", IEEE J. Quantum Electron., 27, pp. 1377-1385, 1991.
- [8] D. Vakhshoori, J. D. Wynn, G. J. Aydzik, R. E. Leibenguth, M. T. Asom, K. Kojima and R. A. Morgan, "Top-surface-emitting lasers with 1.9 V threshold voltage and the effect of spatial hole burning on their transverse mode operation and efficiencies", Appl. Phys. Lett., 62, pp. 1448-1450, 1993.
- [9] R. A. Morgan, M. K. Hibbs-Brenner, R. A. Walterson, J. A. Lehman, T. M. Marta, S. Bounnak, E. L. Kalweit, T. Akinwande and J. C. Nohava, "Producible GaAs-based MOVPE-grown vertical-cavity top-surface emitting lasers with record performance", Electron. Lett., 31, pp. 462-464, 1995.
- [10] C. Degen, I. Fischer, and W. Elsasser, "Thermally induced local gain suppression in vertical-cavity surface-emitting lasers", Appl. Phys. Lett., 76, pp. 3352-3354, 2000.

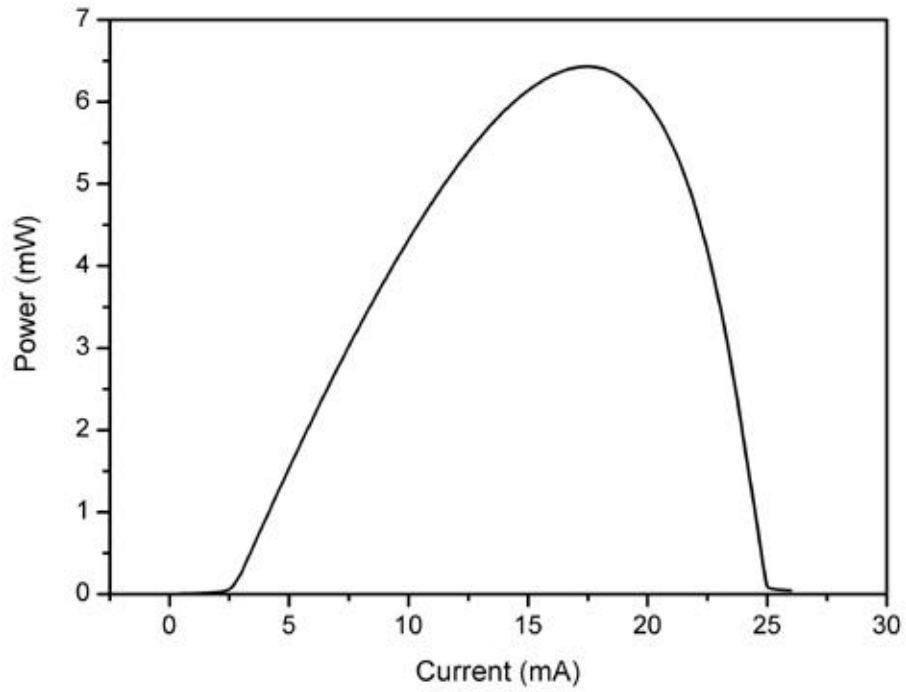


Fig. 3-1 Light output vs. current curve of 20 μm diameter oxide-confined VCSEL under CW operation at room temperature.

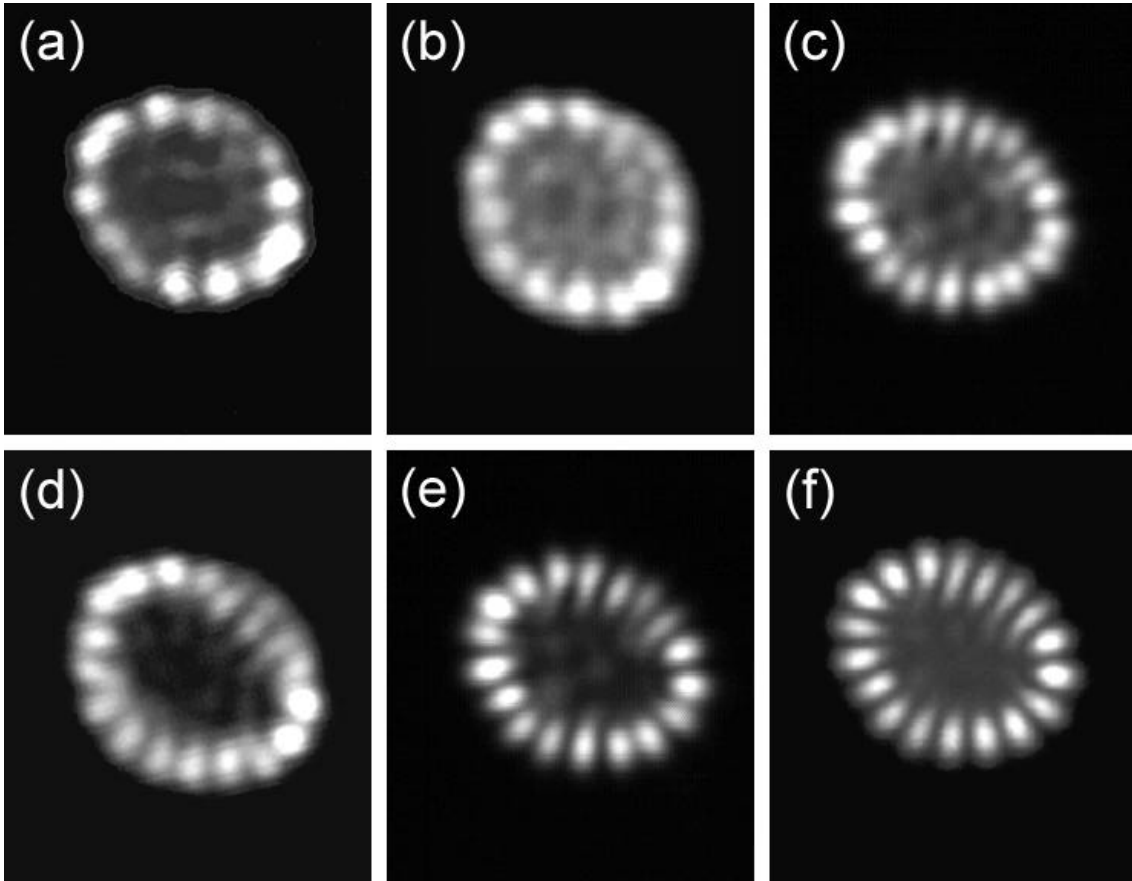


Fig. 3-2 Photographs of near-field patterns of 20 μm diameter oxide-confined VCSEL at injection currents of (a) 10.5 mA, (b) 13.4 mA, (c) 20.0 mA, (d) 22.3 mA, (e) 23.0 mA and (f) 23.3 mA.

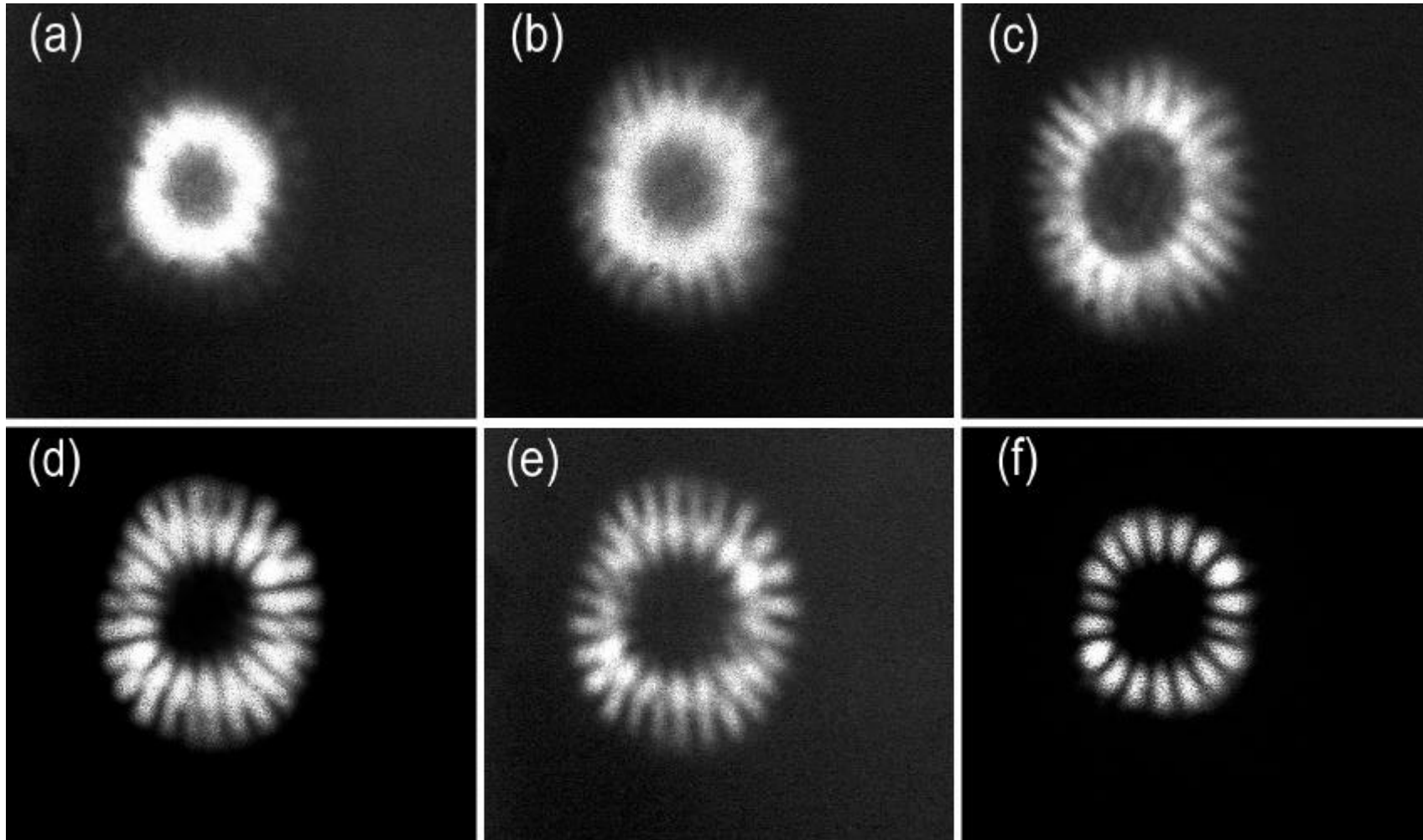


Fig. 3-3 Photographs of far-field patterns of 20 μm diameter oxide-confined VCSEL at injection currents of (a) 10.5 mA, (b) 13.4 mA, (c) 20.0 mA, (d) 22.3 mA, (e) 23.0 mA and (f) 23.3 mA.

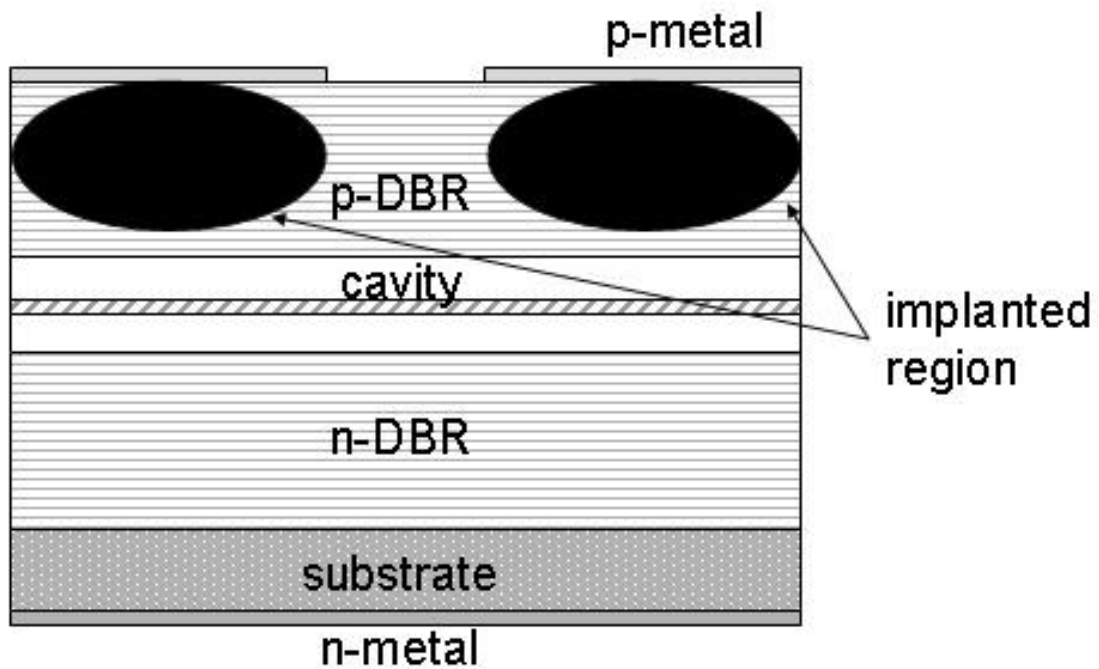


Fig. 3-4 Cross-section sketch of a planar proton-implanted VCSEL with stacked implantation used for electrical isolation.

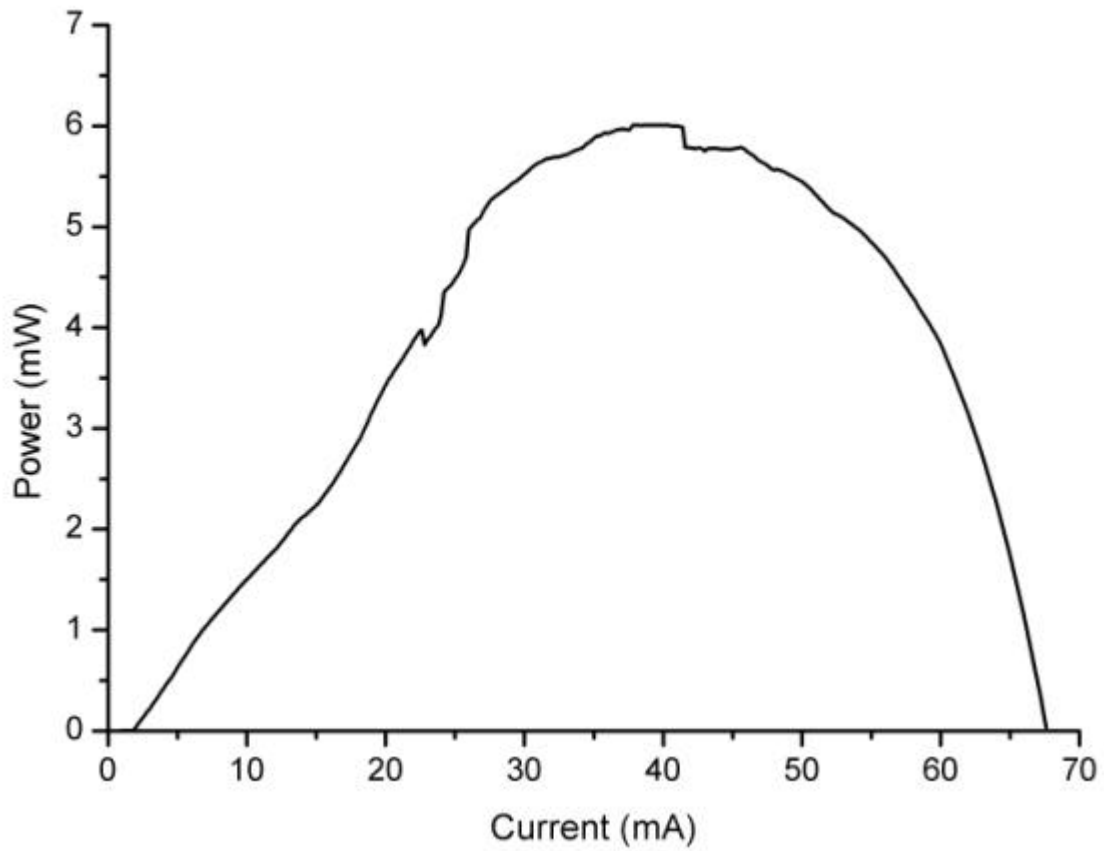


Fig. 3-5 Light output vs. current curve of 20 μm diameter proton-implanted VCSEL under CW operation at room temperature.

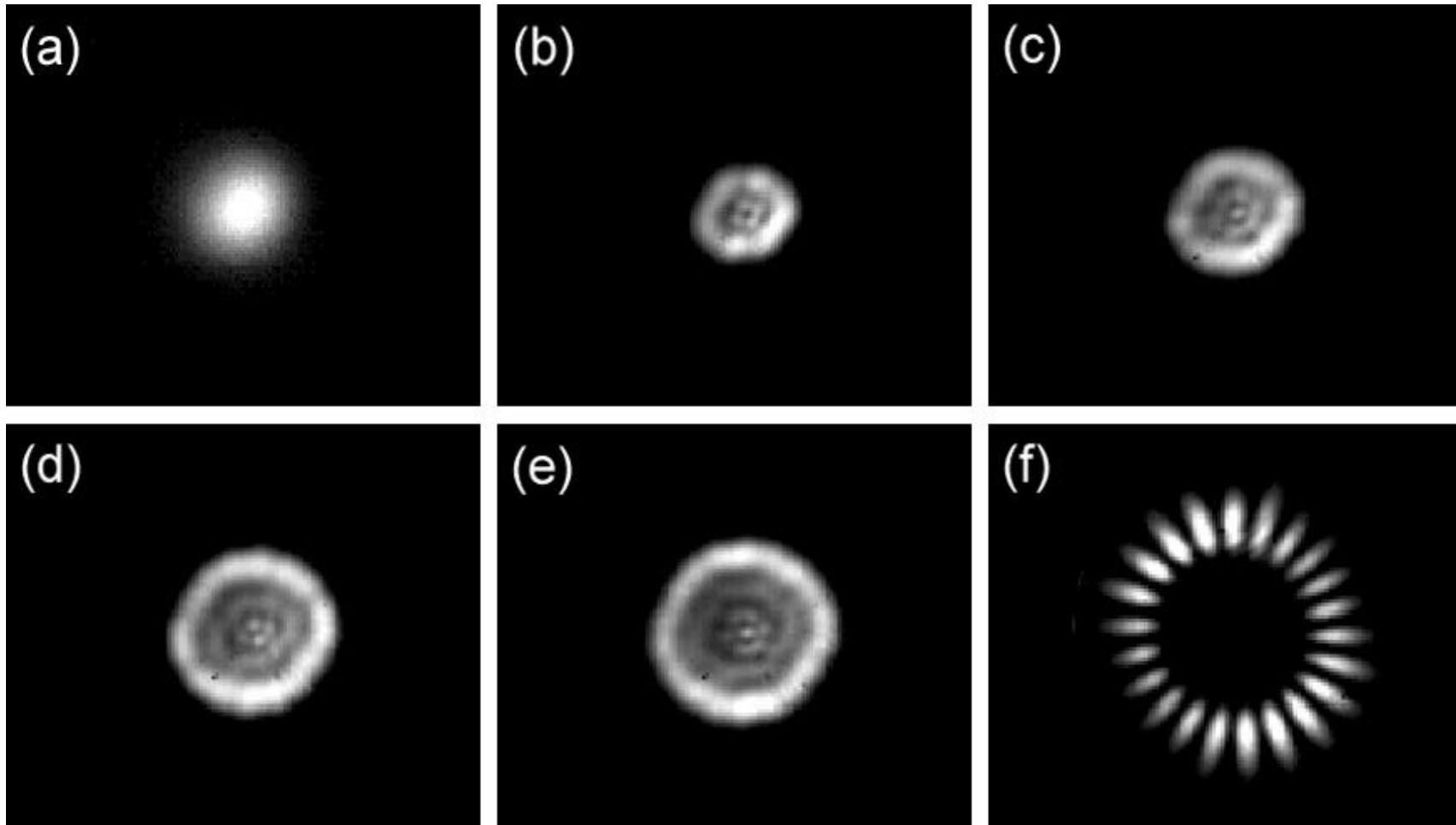


Fig. 3-6 Photographs of far-field patterns of 20 μm diameter proton-implanted VCSEL at injection currents of (a) 4 mA, (b) 17 mA, (c) 24 mA, (d) 34 mA, (e) 41 mA and (f) 59 mA.

Chapter 4. Numerical Simulation of Y-Junction Structured Pattern

4.1 Introduction

In order to provide a quantitative understanding of these emission characteristics, we present a numerical simulation to model and fit the experimental results. The numerical simulation adopts the high-order Laguerre-Gaussian mode due to the assumptions of a parabolic refractive-index profile and ring-shaped carrier distribution in the laser. From the numerical simulation results, the formation of y-junction structures is inferred to be caused by the superposition of two high-order Laguerre-Gaussian modes. The results of this numerical simulation are in good agreement with the experimental findings.

We also solve the guiding modes of cylindrical cavity with parabolic refractive-index profile. The results are consistent with the numerical simulation using LG mode.

The theory of LG mode is presented in section 4.2. In section 4.3, we present the results of the guiding modes of cylindrical cavity with parabolic refractive-index profile. The numerical interpretation of the formation of y-junction structures is then discussed in section 4.4.

4.2 Numerical Model using Laguerre-Gaussian Mode

4.2.1 Theory of Laguerre-Gaussian Mode

We present a numerical simulation for the formation of y-junction structures in a broad-area oxide-confined VCSEL by using the high-order LG mode. The guiding of the mode in oxide-confined VCSELs is generally due to a combination of index guiding, thermal index guiding, and carrier-induced index anti-guiding. Therefore we assume that the refractive index profile in the oxide-confined VCSEL is parabolic and the carriers distribute in a ring shape at the border of the laser. Based on the assumptions, the preferred laser modes in this case are the $LG_{p,l}$ modes. Each degenerate pair (l) of LG modes gives rise to a pair of daisy modes with $2l$ lobes. The normalized intensity distribution of the LG mode is [1]

$$I(r, \mathbf{q}, z) = \left[\frac{4}{l!} \frac{1}{w^2(z)} \left(\frac{2r^2}{w^2(z)} \right)^l \exp\left(-\frac{2r^2}{w^2(z)} \right) \right] \left[\frac{1}{\mathbf{p}} \cos^2(l\mathbf{q}) \right], \quad (4-1)$$

with

$$w^2(z) = w_0^2 \left[1 + \left(\frac{\mathbf{l}z}{\mathbf{p}w_0^2} \right) \right], \quad (4-2)$$

where $w(z)$ is the Gaussian beam waist parameter, w_0 is the beam waist at $z = 0$, and r and \mathbf{q} are the radial and azimuthal coordinate respectively.

From the experimental observations, we adopt the $LG_{0,l}$ modes with $l = 9$ and $l = 13$ to fit the experimental results. Considering the strong optical confinement provided by the oxidized layer, we also assume the beam waist of the $LG_{0,9}$ and $LG_{0,13}$ mode are similar in near-field.

4.2.2 Numerical Results

Experimental near-field images of the 20 μm diameter oxide-confined VCSEL are presented in Fig. 4-1, and corresponding spectrum is shown in Fig. 4-2. While the injection current is 22.3 mA, which is larger than the thermal roll-over point, the high-intensity distribution can only be observed around the periphery of the oxide aperture as shown in Fig. 4-1(a). The laser is operated in multi transverse modes according to the corresponding spectrum in Fig. 4-2(a). These two results indicate that the multiple high-order transverse modes tend to gather around the periphery of the oxide aperture due to a strong optical confinement induced by the oxidized layers. Therefore the y-junction structured pattern cannot be observed in the near-field images. At an even larger injection current of 23.3 mA, the lasing near-field pattern becomes a pure single high-order mode which has 18 spots as shown in Figs. 4-1(b) and 4-2(b).

We present the far-field intensity distribution in Fig. 4-3, which contains the 180°-rotation symmetrical images at injection currents of 22.3 mA (a) and 23.3 mA (b). The y-junction structured pattern is observed in Fig. 4-3(a) and a 9th-order daisy mode is observed in Fig. 4-3(b). Since the lasing modes of the VCSEL at 22.3 mA are multiple transverse modes

according to Fig. 4-2(a) and these high-order transverse modes have similar divergent angles in far-field emission as shown in Fig. 4-3(a), we conclude that the interaction between the adjacent high-order transverse modes induces the formation of the y-junction structured pattern.

The numerical results of near-field intensity distribution are shown in Fig. 4-4, which contains the superposition of two high-order LG modes ($LG_{0,9}$ and $LG_{0,13}$ mode) in Fig. 4-4(a), and the single high-order mode ($LG_{0,9}$ mode) in Fig. 4-3(b). The result in Fig. 4-4(b) implies that the $LG_{0,13}$ mode is suppressed due to thermal detuning between the cavity resonance and the QW spectral gain maximum [2]. The corresponding far-field images are presented in Fig. 4-5. Fig. 4-5(a) is the calculated result of the intensity distribution of the superposition of 9th-order and 13th-order LG mode, and Fig. 4-5(b) is the intensity distribution of a 9th-order LG mode. In far-field, the beam waist $w(z)$ increases with the distance z , then the superposition of two high-order LG modes turns to a different pattern comparing to the near-field pattern, as can be seen in Fig. 4-5(a). This numerical simulation result demonstrates that the formation of y-junction structures is induced by the superposition of two high-order LG mode with similar divergent angles.

4.3 Guiding Mode of Cylindrical Cavity

4.3.1 Theory

Assuming that our waves have harmonic time dependence, we use the reduced wave equation in the form

$$\nabla^2 \mathbf{y} + n^2 k_0^2 \mathbf{y} = 0 \quad (4-3)$$

with the free space propagation constant

$$k_0 = \omega \sqrt{\epsilon_0 \mu_0} = \frac{2\pi}{\lambda} \quad (4-4)$$

The guiding of the mode in oxide-confined VCSELs is generally due to a combination of index guiding, thermal index guiding, and carrier-induced index anti guiding. Therefore we assume that the refractive-index profile in the oxide-confined VCSEL is parabolic

$$\begin{aligned} n^2 &= n_1^2 - n_1 n_2 (x^2 + y^2) = n_1^2 \left(1 - \frac{r^2}{l^2} \right) & 0 \leq r \leq r_a \\ n &= n_2 & r \geq r_a \end{aligned} \quad (4-5)$$

$$l = \frac{r_a}{\sqrt{1 - (n_2/n_1)^2}}$$

where r_a is the diameter of the oxidized aperture. In polar coordinates, the wave equation can be expressed as

$$\frac{1}{r} \frac{\partial}{\partial r} \left(r \frac{\partial \mathbf{y}}{\partial r} \right) + \frac{1}{r^2} \frac{\partial^2 \mathbf{y}}{\partial \mathbf{f}^2} + \frac{\partial^2 \mathbf{y}}{\partial z^2} + n^2(r) k_0^2 \mathbf{y} = 0 \quad (4-6)$$

Since the refractive index is a function of r only, we can separate the solution into a product of r -dependent, f -dependent and z -dependent solutions:

$$\mathbf{y}(r, \mathbf{f}, z) = u_r(r) u_f(\mathbf{f}) u_z(z) \quad (4-7)$$

Then eq. (4-6) can be transformed to

$$\frac{d^2 u_r}{dr^2} + \frac{1}{r} \frac{du_r}{dr} + \left[n^2(r) k_0^2 - \frac{m^2}{r^2} - \mathbf{b}^2 \right] u_r = 0 \quad (4-8)$$

where \mathbf{b} is the propagation constant in z direction, and the f dependence of the solution will be of the form $\exp[\pm im\mathbf{f}]$.

A proper trial function is the following form [3]

$$u_r(r) = r^{|m|} e^{-\frac{C}{2}r^2} F(r) \quad (4-9)$$

where

$$C = \frac{n_1 k_0}{l} \quad (4-10)$$

where $F(r)$ is a yet unknown function of r . With this trial function, after tedious manipulation, a different equation for $F(t)$, where also a change of variable r to $t = Cr^2$ is done, is obtained:

$$tF'' + [(|m| + 1) - t]F' - \left[\frac{1}{2}(|m| + 1) - \frac{E}{4C} \right] F = 0 \quad (4-11)$$

where

$$E = n_1^2 k_0^2 - \mathbf{b}^2 \quad (4-12)$$

Note that the variable t is not time.

This eq. (4-11) is of the type of the so-called Kummer's equation (also known as a confluent hypergeometric equation) [4]

$$xy''(x) + (c - x)y'(x) - ay(x) = 0 \quad (4-13)$$

where one now has $x \equiv t, c \equiv (|m| + 1)$ and $a \equiv \left[\frac{1}{2}(|m| + 1) - \frac{E}{4C} \right]$. Kummer's equation has a regular singularity at $x = 0$ and an irregular singularity in $x = \infty$, which means that the solution F is not square integrable in general i.e. it cannot be normalized.

One solution of Kummer's equation is Kummer's function :

$$y(x) = F_1(a, c; x) = 1 + \frac{ax}{c!} + \frac{a(a+1)x^2}{c(c+1)2!} + \frac{a(a+1)(a+2)x^3}{c(c+1)(c+2)3!} + \dots \quad (4-14)$$

From this solution one notices that, if a is any of the values $a = 0, -1, -2, \dots$, the series stops at some term. Hence it is possible to truncate the Kummer's function series and normalize it. One should notice that this requires also that $c \neq 0, -1, -2, \dots$, since then some of the divisors would be zero. But this condition is automatically fulfilled by $c \equiv (|m| + 1) \geq 1$. Now, in order for the

solutions y to be square integrable, one must write the following condition for a :

$$a \equiv \left[\frac{1}{2}(|m| + 1) - \frac{E}{4C} \right] = -n \quad (4-15)$$

where $n = 0, 1, 2, \dots$. The eigenfunctions of eq. (4-6) are

$$y_{nm}(r, \mathbf{f}, z) = B_{nm} r^{|m|} e^{-\frac{C}{2}r^2} F_1\left(-n, |m| + \frac{1}{2}; Cr^2\right) e^{im\mathbf{f}} e^{ibz} \quad 0 \leq r \leq r_a \quad (4-16)$$

where $F_1\left(-n, |m| + \frac{1}{2}; Cr^2\right)$ is the confluent hypergeometric function of the first kind and B_{nm} is the normalizing factor.

The refractive index of the buried oxide layer changes from ~ 3.0 for the original AlGaAs layer to ~ 1.6 for the oxidized layer, which induces a significant index difference between the laser cavity and the region surrounding the cavity. This boundary effect strongly confine the optical field with the cavity, therefore we assume that the optical field is zero at $r = r_a$. With this boundary condition, the corresponding eigenvalues derived from eq. (4-16) are $n = 0, 1, 2, \dots$ and $m = 0, \pm 1, \pm 2, \dots$

4.3.2 Numerical Results

We present the first three eigen-values and corresponding eigen-functions in Fig. 46. The results are similar to the 2-D harmonic oscillator in quantum mechanism. The numerical results of near-field intensity distribution are shown in Fig. 4-7, which contains the superposition of two high-order modes ($y_{0,9}$ and $y_{0,13}$ mode) in Fig. 4-7(a), and the single high-order mode ($y_{0,9}$ mode) in Fig. 4-7(b). The corresponding far-field images are presented in Fig. 48. Fig. 4-8(a) is the calculated result of the intensity distribution of the superposition of 9th-order and 13th-order $y_{0,m}$ mode, and Fig. 4-8(b) is the intensity distribution of a 9th-order $y_{0,m}$ mode.

4.4 Discussions

In previous studies, high-order LG modes usually show up in board-area VCSELs at large injection currents [5]. Moreover, the tendency to emit multi-high-order modes in board-area VCSELs appears to be stronger than in the small-area ones because the inhomogeneous carrier distribution and thermal gradient become more pronounced at the perimeter in larger devices [2,5-6]. Based on the previous studies and our experimental observations in Fig. 4-1(b) and 4-2(b), we adopt the high-order LG mode in our simulations with assumptions of the parabolic refractive index profile and the ring-shaped carrier distribution.

The ideal VCSEL structure (plano-planar resonator configuration and flat gain, and refractive index distribution in the active zone surrounded by

an index step due to the oxide aperture) should support so-called linearly polarized modes (LP modes), analogous to the ones known from step-index fibers. However, the radial variation of the carrier distribution and the creation of an inhomogeneous temperature profile by ohmic heating will result in some amount of self-focusing in the laser via the dependence of the refractive index on carrier density and temperature. This self-focusing effect can be approximated by parabolic refractive index profile. Additionally, a strong carrier confinement provided by the oxidized layers, the current spreading, and the thermal gradients are the dominant mechanisms governing the carrier distribution in the active region of the oxide-confined VCSELs. The combination of these effects causes the carriers distribute within a ring-shaped area in the perimeter of the active region. Therefore the parabolic refractive index profile and the ring-shaped carrier distribution are the reasonable assumption, and the Laguerre-Gaussian mode is the appropriate eigen-function to explain the experiment observations.

According to the experimental and simulation results, the transverse modes with y-junction structures can be observed in far-field images at 22.3mA, which is higher than thermal roll-over point, and they are formed by two superposed high-order LG modes, $LG_{0,9}$ and $LG_{0,13}$, emitting with similar divergent angles. These multi-high-order modes are confined within the oxide aperture due to the strong optical confinement so that the details of the transverse modes and the y-junction structured pattern cannot be observed in near-field images. At an even larger injection current of 23.3mA, only $LG_{0,9}$ can be seen because $LG_{0,13}$ is suppressed. The large divergence of the $LG_{0,13}$ in far-field corresponds to a larger transverse

component of the k vector compared to $LG_{0,9}$. The preference of $LG_{0,9}$ is basically determined by the thermal detuning between the cavity resonance and the QW spectral gain maximum: the high-order modes with longer wavelength ($LG_{0,9}$) more efficiency exploit the optical gain and high-order modes with shorter wavelength ($LG_{0,13}$) are suppressed at large injection current. The thermal shift of the emission wavelength at large injection current is determined by the thermal expansion of the cavity and the thermal increase of the optical index. From the simulation results, we also conclude that the laser supports extremely high-order modes of $LG_{0,9}$ and $LG_{0,13}$. The emission of such high-order modes, even in an electrically pumped VCSEL, can be only possible if the processed wafer is extraordinarily homogeneous.

References

- [1] S. F. Pereira, M. B. Willemsen, M. P. van Exter and J. P. Woerdman, “Pinning of daisy modes in optically pumped vertical-cavity surface-emitting lasers”, Appl. Phys. Lett., 73, pp. 2239-2241, 1998.
- [2] C. Degen, I. Fischer, W. Elsasser, L. Fratta, P. Debernardi, G. P. Bava, M. Brunner, R. Hovel, M. Moser and K. Gulden, “Transverse modes in thermally detuned oxide-confined vertical-cavity surface-emitting lasers”, Phys. Rev. A, 63, pp. 023817/1-12, 2001.
- [3] Siegfried Flugge, Practical Quantum Mechanics, Springer International, Berlin Heidelberg, 1971.
- [4] George Arfken, Mathematical Methods for Physicists, Academic Press INC., 1985.
- [5] C. Degen, B. Krauskopf, G. Jennemann, I. Fischer and W. Elsasser, “Polarization selective symmetry breaking in the near-fields of vertical cavity surface emitting lasers.”, J. Opt. B: Quantum & Semiclassical Opt., 2, pp. 517-525, 2000.
- [6] T. Ackemann, S. Barland, M. Cara, S. Balle, J. R. Tredicce, R. Jager, M. Grabherr, M. Miller and K. J. Ebeling, “Spatial mode structure of bottom-emitting broad-area vertical-cavity surface-emitting lasers”, J. Opt. B: Quantum & Semiclassical Opt., 2, pp. 406-412, 2000.

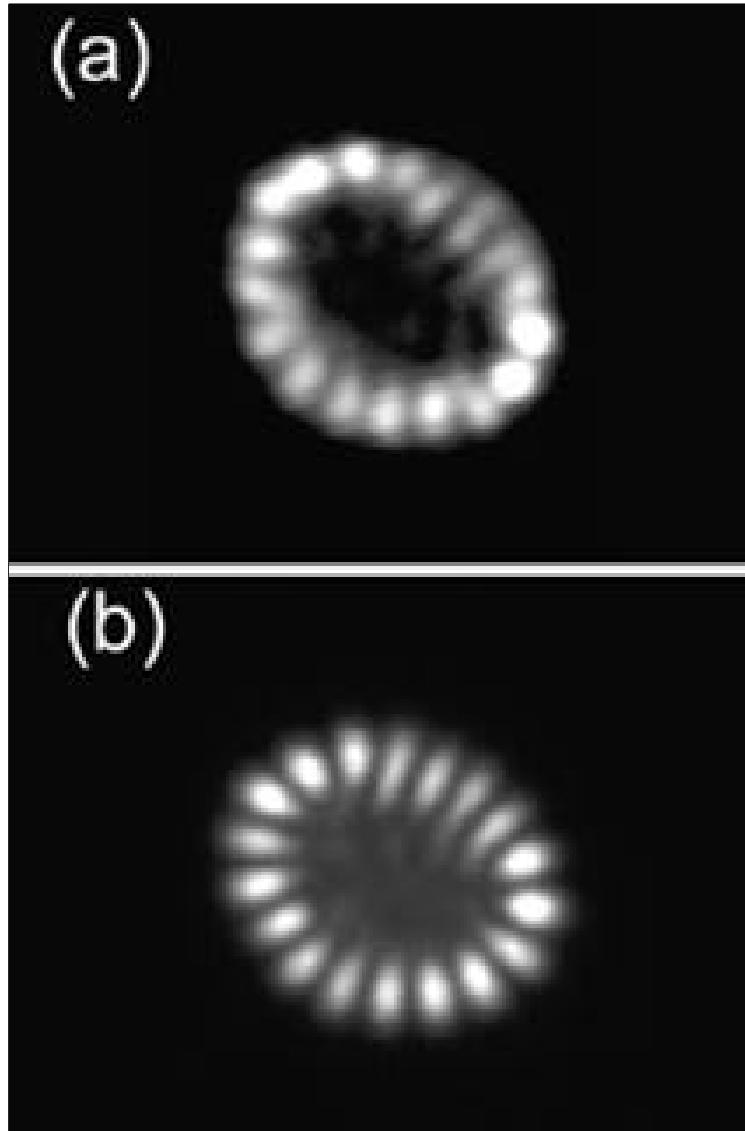


Fig. 4-1 Photographs of experimental near-field patterns of 20 μm diameter oxidized VCSEL at injection currents of (a) 22.3 mA, (b) 23.3 mA.

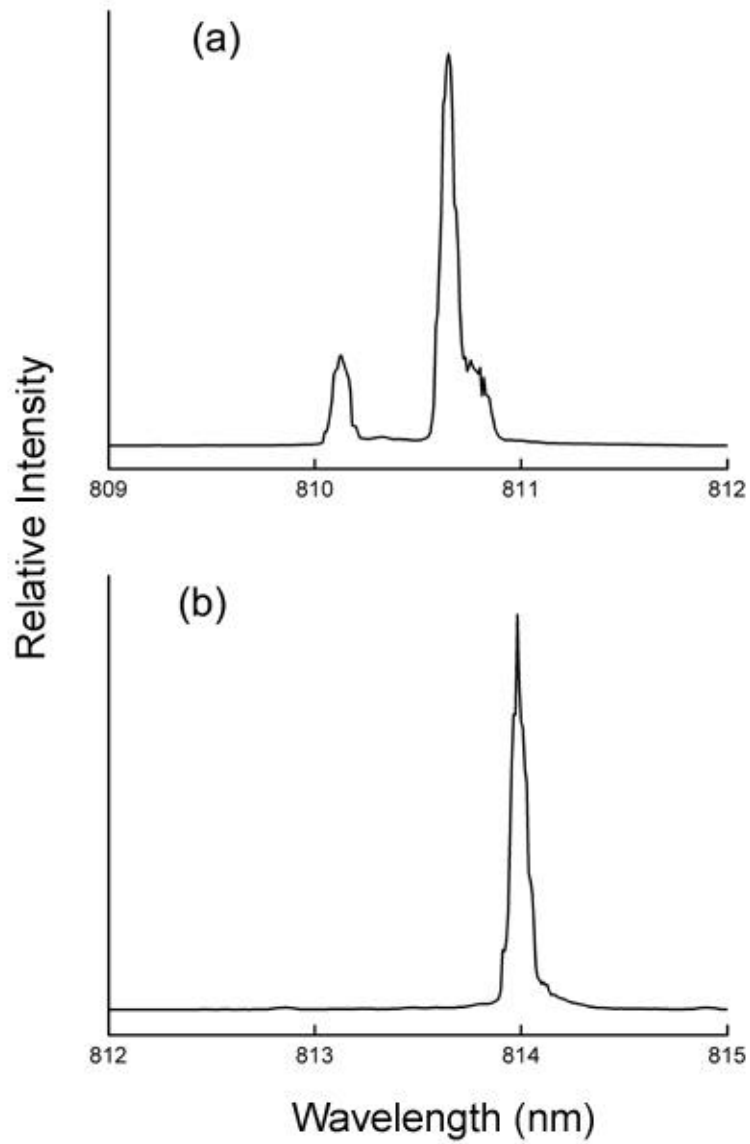


Fig. 4-2 Spectral data of 20 μm diameter oxide-confined VCSEL at injection currents of (a) 22.3 mA and (b) 23.3 mA.

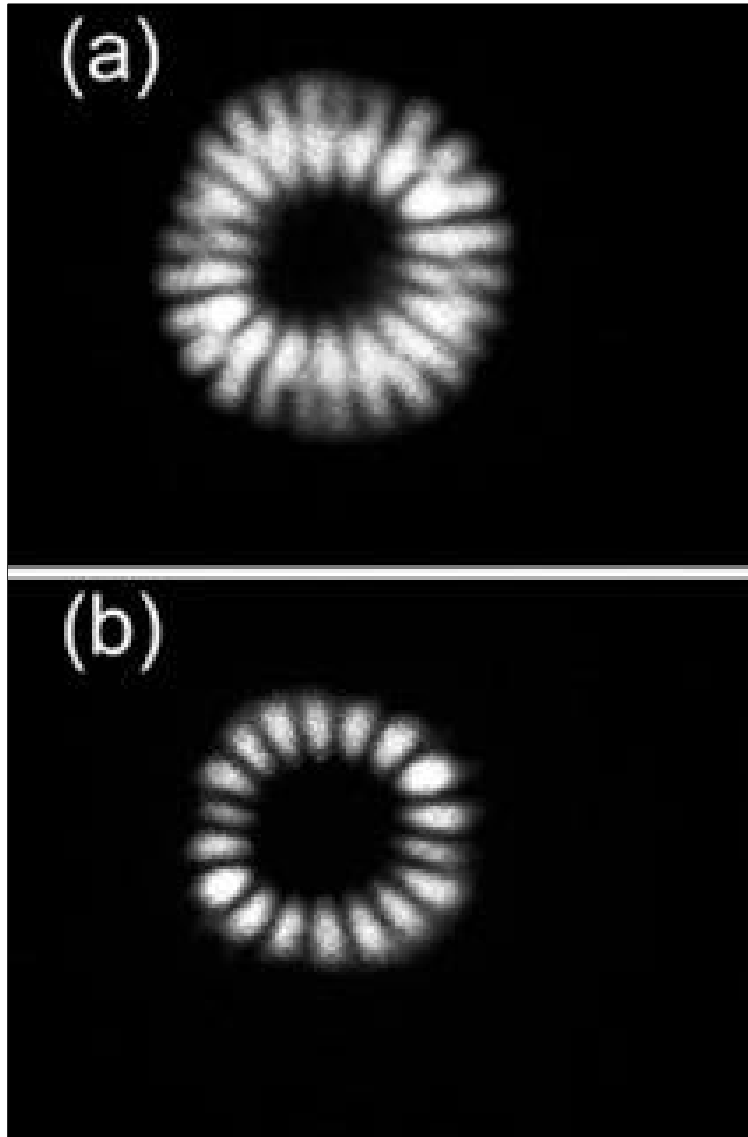


Fig. 4-3 Photographs of experimental far-field patterns of 20 μm diameter oxidized VCSEL at injection currents of (a) 22.3 mA, (b) 23.3 mA.

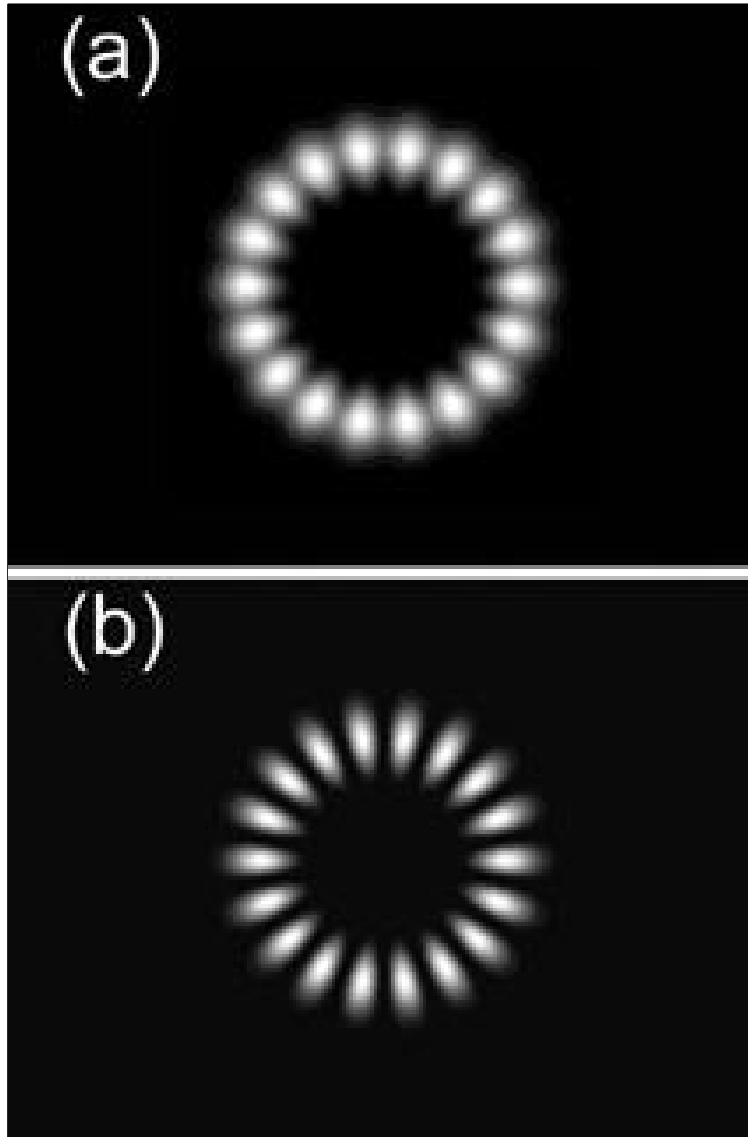


Fig. 4-4 Computer calculated near-field patterns corresponding to Fig. 4-1 for 20 μm diameter oxidized VCSEL.

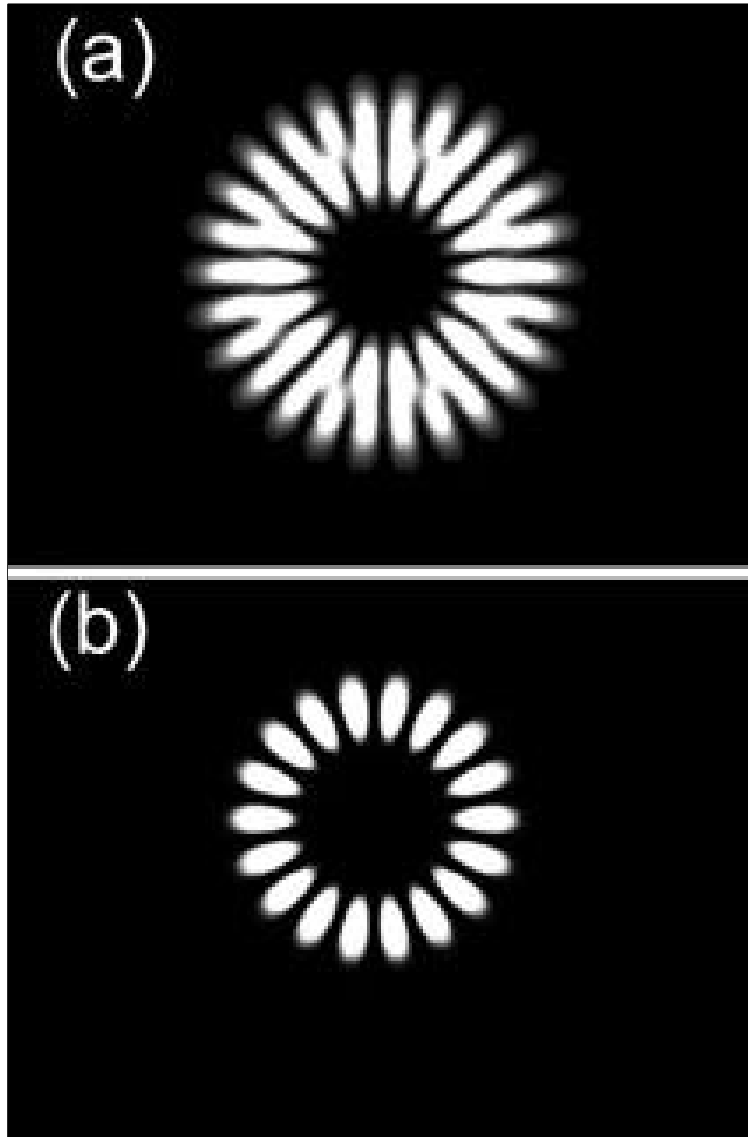


Fig. 4-5 Computer calculated far-field patterns corresponding to Fig. 4-2 for 20 μm diameter oxidized VCSEL.

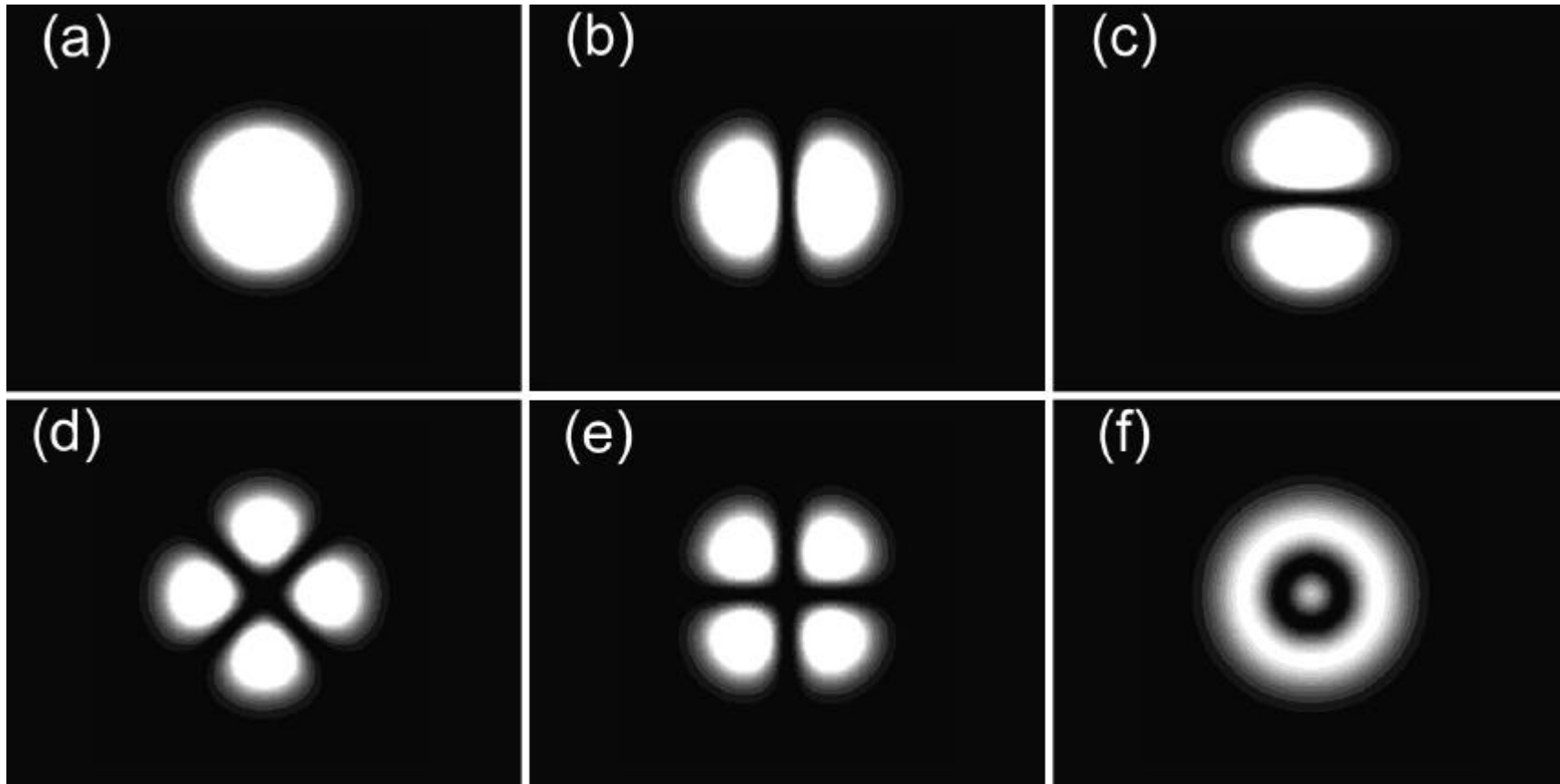


Fig. 4-6 First three eigen-values and corresponding eigen-functions with (a) $n = 0, m = 0$; (b) $n = 0, m = 1$; (c) $n = 0, m = -1$; (d) $n = 0, m = 2$; (e) $n = 0, m = -2$; (f) $n = 1, m = 0$.

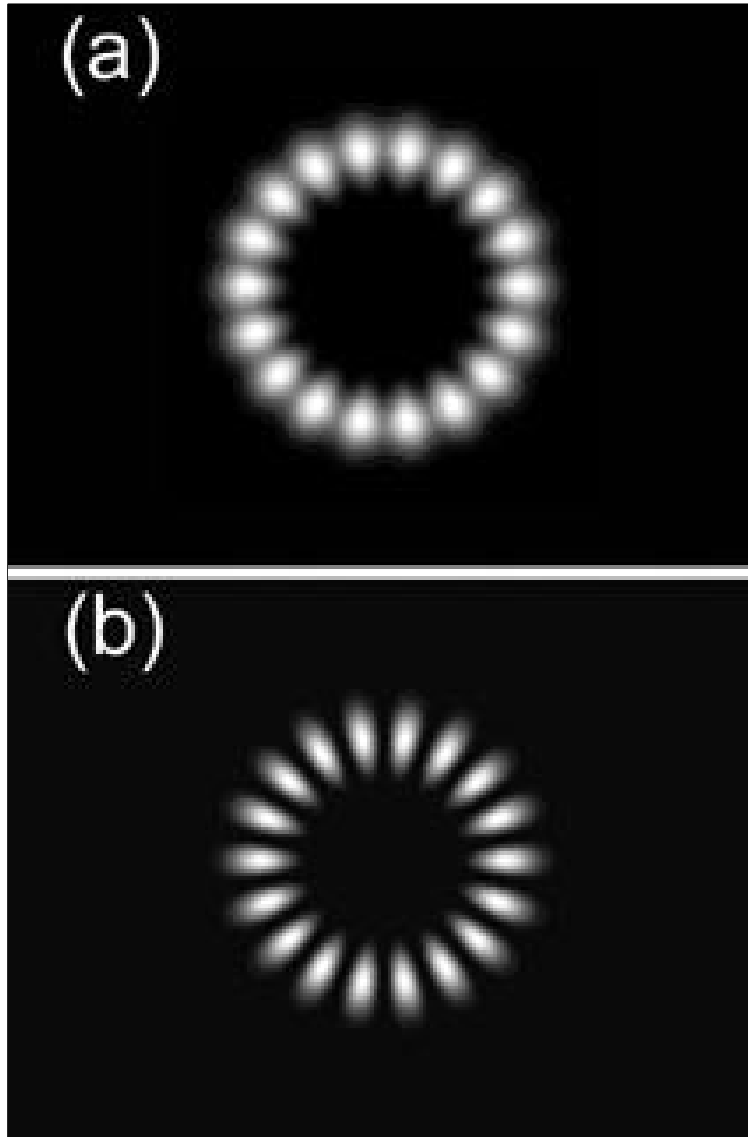


Fig. 4-7 Computer calculated near-field patterns corresponding to Fig. 4-1 for 20 μm diameter oxidized VCSEL.

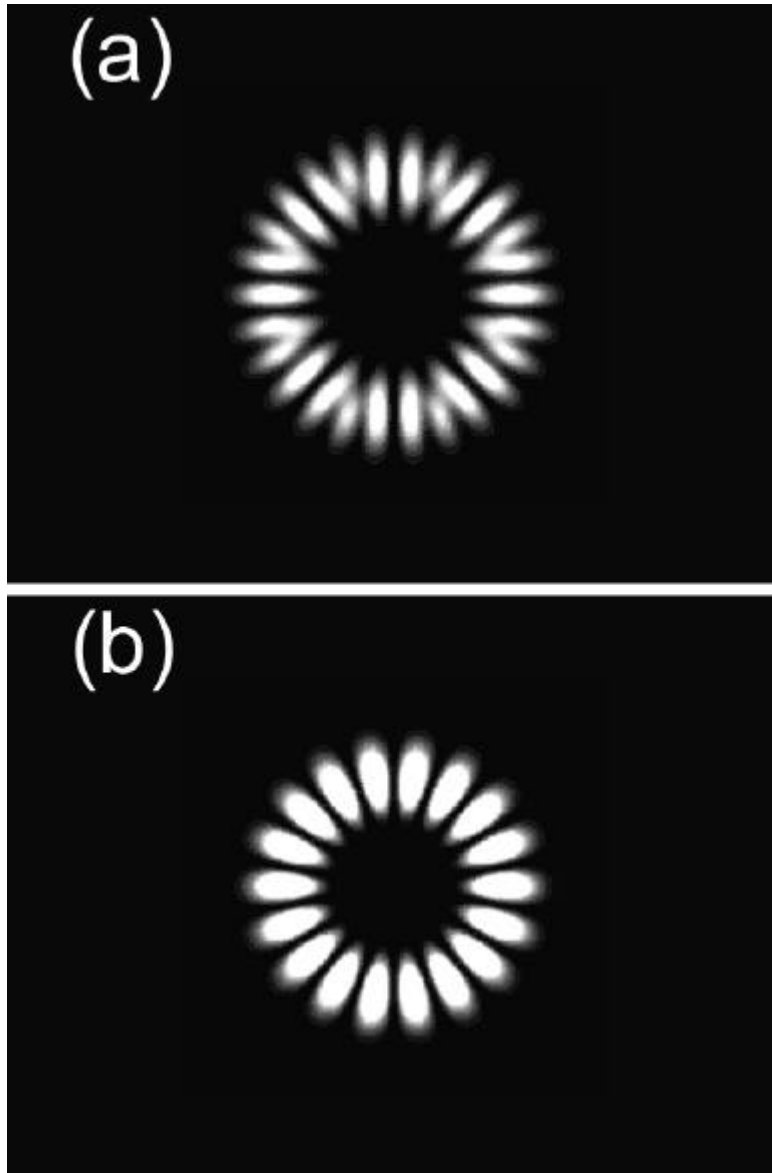


Fig. 4-8 Computer calculated far-field patterns corresponding to Fig. 4-2 for 20 μm diameter oxidized VCSEL.

Chapter 5. Conclusions

5.1 Introduction

In this chapter, our aim is to distinguish between the influences that different effects such as inhomogeneous carrier distribution, nonuniform thermal gradients and boundary effect induced by oxidized layers have on the transverse modal behaviour of broad area oxide-confined VCSELs. The combination of these complex effects then results in the preference of multi-high-order transverse modes in the lasers.

The contribution of inhomogeneous carrier distribution to the transverse mode of broad area oxide-confined VCSEL is presented in section 5.2. In section 5.3, we discuss the influence of thermal effects to the transverse mode. The boundary effects are then described in section 5.4. The contribution to the formation of y-junction structures are shown in section 5.5 and our interpretation is compared with numerical simulation presented in chapter 4. The last section summarizes the results of this chapter.

5.2 Inhomogeneous Carrier Distribution

From the results of our experimental investigations, we conclude that the observed emission characteristics are determined by inhomogeneous carrier distribution, nonuniform thermal gradients and boundary effect induced by oxidized layers. In the VCSELs of larger active regions, the current is only practically flowing within a narrow annular area close to the perimeter of the confinement region, and current of such a distribution does

reach the active region. This inhomogeneous carrier distribution arises purely from the current flow through the confinement area and not from an interaction with optical fields in the cavity. This conclusion is supported by the results of theoretical simulations by Nakwaski [1] and experimental measurements by Degen et al. [2]. Nakwaski performed numerical calculations on the transverse spreading of the injection current in proton-implanted VCSELs independently from the influence of optical fields inside the cavity. The modeling resulted in distributions of the current density inside the carrier confinement region that showed distinct maxima at the borders of the VCSEL and a deep dip in the center. These distributions are in good agreement with the experimental results [2], which show at all injection currents for VCSELs a corresponding shape with maxima at the periphery and a broad minimum in the center. This distribution causes obviously a strong tendency towards the emission of high order modes, which efficiently benefit from the inhomogeneous spatial gain distribution which produces more optical gain at the periphery of the active region than in the centre. The good agreement of the theoretical results for the proton-implanted VCSEL and experimental results obtained from oxide-confined devices are quite remarkable since one of the major differences between these structures is the stronger carrier confinement by the oxidized layers.

5.3 Thermal Effects

The tendency to high order mode emission is further enhanced by strong thermal gradients in the cavity. These gradients have also been modeled and temperature differences larger than 30K have been predicted

between the center and the border region of the VCSEL [3]. The temperature differences origin from Joule-heating and heating by non-radiating recombination processes. Thus, the temperature differences will be highest for injection currents larger than the thermal roll-over point, because then the injection current is already high and non-radiating recombination strongly increases. As a consequence of this thermal gradient, carriers will be thermally excited and re-distributed towards higher energies. This effect of spectral carrier re-distribution is of course stronger in the hot center of the VCSEL and weaker at the cooler periphery. In a small energy interval, as it is selected by the interference filters at the wavelength of spontaneous emission but as well by the VCSELs' Bragg-reflector at the lasing wavelength, the strong re-distribution of carriers in the center of the VCSEL will obviously lead to a broad dip in the carrier distribution. This behaviour is interpreted as a direct consequence of the strong thermal gradients. Only with this additional mechanism, a particularly tailored gain distribution can occur, that is very similar to the 'doughnut' shaped optically pumped setup by Pereira [4]. Consequently, very similar daisy-modes can be observed in this electrically pumped setup, with the order of the modes even exceeding the ones observed in the optically pumped VCSEL.

In principle, thermal effects in a VCSEL can show up in a two fold manner: besides local gain suppression, which favors higher order modes, thermal lensing has been identified to confine the optical field in small aperture VCSELs and, therefore, favors single mode emission [5]. Thermal lensing is the dominant thermal effect for low to intermediate-injection currents, while local gain suppression determines the emission

characteristics at high injection currents, even in comparably small devices. At high injection currents, pump-induced heating leads to local gain suppression in the center of VCSELs [6]. This effect overbalances thermal lensing, thus, a strong tendency towards the emission of high order modes has been found, because those mode profiles better match the modified spatial gain profile.

5.4 Boundary Effects

Selectively oxidized VCSELs are strongly index-guided, which profoundly influences the optical characteristics such as transverse mode behaviour. The lateral boundary conditions in the oxide-confined VCSELs are determined by buried native-oxide layer to provide the transverse mode confinement along the circular perimeter. The refractive index of the buried oxide layer changes from ~ 3.0 for the original AlGaAs layer to ~ 1.6 for the oxidized layer [7,8], which induces a significant index difference between the laser cavity and the region surrounding the cavity [9,10]. Thus, the reflectivity of the upper mirror is locally increased due to the enhanced contrast between the optical indexes of the adjacent layers. This local higher reflectivity is more efficient on the higher-order modes that exhibit complex flower-like structures. Moreover, high contrast ratio of refractive index causes VCSELs tend to emit multiple optical transverse modes.

The boundary effects supported by oxidized layers strongly confine the carrier and multiple high order optical transverse modes within the laser cavity. The improved electrical confinement afforded by buried oxide apertures is evident in the lower threshold voltage of selectively oxidized VCSELs as compared to other device structures [11,12]. The index-guiding

optical confinement is obtained as evident from the low threshold current [13,14] and the VCSEL emission characteristics [9,10]. A strong optical confinement introduced by the oxidized layers causes the multiple high-order transverse modes to gather around the periphery of the oxide aperture so that the detail structures of transverse modes cannot be observed in near-field.

5.5 Y-Junction Structured Pattern

The y-junction structured pattern is extensively observed in studies of pattern formation [15-17]. One of the complex dynamics that govern these patterns is perhaps the occurrence of instabilities and symmetry breaking. In lasers, the y-junction structured pattern observed so far was in the interferogram of optical vortices [18,19]. The interference fringe with y-junction structured pattern is called “edge phase dislocation” [18] or “forks” [19]. For the broad-area oxide-confined VCSEL, the y-junction structured pattern can only be observed in the far-field emission. The adjacent high-order transverse modes with similar divergent angles induce an interaction which causes the formation of the y-junction structures.

For the numerical simulation, we assumed a parabolic refractive-index profile and ring-shaped carrier distribution in the laser. Therefore, we adopted the high-order LG modes to model and fit the experimental observations. The formation of the transverse mode with y-junction structures is the result of the superposition of $LG_{0,9}$ and $LG_{0,13}$ modes, according to the numerical calculation. We concluded, on the basis of the numerical simulation results, that the inhomogeneous carrier distribution and temperature profile are particularly attractive for building cavities that

preferentially operate with multiple high-order modes, leading to the formation of y-junction structures. The results of our simulations provide a theoretical explanation of the experimental behavior.

5.6 Summary

We have presented experimental and numerical investigations of the emission behavior of the 20 μm in diameter, oxide-confined VCSEL while the operation current is from near threshold current to well above the thermal roll-over point. The near-field images shows that the strong optical confinement introduced by the oxidized layers causes the high-order modes tend to crowd around the periphery of the oxide aperture so that the y-junction structured pattern cannot be observed. The transverse mode with y-junction structures can only be observed in far-field images. To distinguish the influence of different guiding mechanisms on the transverse modal behavior, we compare the experimental results of a 20 μm diameter aperture oxide-confined VCSEL to a proton-implanted VCSEL. We conclude that the emission behavior of large-sized oxide-confined VCSEL is determined by the combined effect of the inhomogeneous carrier distribution, nonuniform thermal gradient and the oxide-layer-specific optical confinement.

For the numerical simulation, we assume the parabolic refractive index profile and ring-shaped carrier distribution in the laser. Therefore we adopt the high-order LG modes to fit the experimental observations. The formation of the transverse mode with y-junction structures is the result of the superposition of $\text{LG}_{0,9}$ and $\text{LG}_{0,13}$ mode according to the numerical calculation. We conclude from the numerical simulation results that the

inhomogeneous carrier distribution and temperature profile can be especially attractive to build cavities that preferentially select multi-high-order mode operation leading to the formation of y-junction structures. The results of our simulations provide theoretical interpretation of the experimental behavior.

References

- [1] W. Nakwaski, “Current spreading and series resistance of proton-implanted vertical-cavity top-surface-emitting lasers”, Appl. Phys. A, 61, pp. 123-127, 1995.
- [2] C. Degen, I. Fischer, and W. Elsasser, “Transverse modes in oxide confined VCSELs: influence of pump profile, spatial hole burning, and thermal effects”, Opt. Exp., 5, pp. 38-47, 1999.
- [3] W. Nakwaski and R. P. Sarzala, “Transverse modes in gain-guided vertical-cavity surface-emitting lasers”, Opt. Commun., 148, pp. 63-69, 1998.
- [4] S. F. Pereira, M. B. Willemsen, M. P. van Exter and J. P. Woerdman, “Pinning of daisy modes in optically pumped vertical-cavity surface-emitting lasers”, Appl. Phys. Lett., 73, pp. 2239-2241, 1998.
- [5] M. Brunner, K. Gulden, R. Hovel, M. Moser, and M. Illegems, “Thermal lensing effects in small oxide confined vertical-cavity surface-emitting lasers”, Appl. Phys. Lett., 76, pp. 7-9, 2000.
- [6] C. Degen, I. Fischer, and W. Elsasser, “Thermally induced local gain suppression in vertical-cavity surface-emitting lasers”, Appl. Phys. Lett., 76, pp. 3352-3354, 2000.
- [7] C. W. Wilmsen, H. Temkin, and L. A. Coldren, Vertical-cavity surface-emitting lasers: design, fabrication, characterization, and applications, Cambridge university press, New York, 1999.
- [8] F. A. Kish, S. J. Caracci, N. Holonyak, Jr., J. M. Dallesasse, K. C. Hsieh, M. J. Ries, S. C. Smith, and R. D. Burnham, “Planar native-oxide index-guided $\text{Al}_x\text{Ga}_{1-x}\text{As}$ -GaAs quantum well

- heterostructure lasers”, Appl. Phys. Lett., 59, pp. 1755-1757, 1991.
- [9] D. L. Huffaker, J. Shin, and D. G. Deppe, “Lasing characteristics of low threshold microcavity lasers using half-wave spacer layers and lateral index confinement”, Appl. Phys. Lett., 66, pp. 1723-1725, 1995.
- [10] K. L. Lear, K. D. Choquette, R. P. Schneider, Jr., and S. P. Kilcoyne, “Modal analysis of a small surface emitting laser with a selectively oxidized waveguide”, Appl. Phys. Lett., 66, pp. 2616-2618, 1995.
- [11] K. D. Choquette, K. M. Geib, C. I. H. Ashby, R. D. Twesten, O. Blum, H. Q. Hou, D. M. Follstaedt, B. E. Hammons, D. Mathes, and R. Hull, “Advances in selective oxidation of AlGaAs alloys”, J. Special Topics of Quantum Electron., 3, pp. 916-926, 1997.
- [12] K. D. Choquette, K. L. Lear, R. P. Schneider, Jr., and K. M. Geib, “Cavity characteristics of selectively oxidized vertical-cavity lasers”, Appl. Phys. Lett., 66, pp. 3413-3415, 1995.
- [13] D. L. Huffaker, D. G. Deppe, K. Kumar, and T. J. Rogers, “Native-oxide defined ring contact for low threshold vertical-cavity lasers”, Appl. Phys. Lett., 65, pp. 97-99, 1994.
- [14] G. M. Yang, M. H. MacDougal, and P. D. Dapkus, “Ultralowthreshold current vertical-cavity surface-emitting lasers obtained with selective oxidation”, Electron. Lett., 31, pp. 886-888, 1995.
- [15] S. Ciliberto, E. Pampaloni and C. Perez-Garcia, “Competition between Different Symmetries in Convective Patterns”, Phys. Rev. Lett., 61, pp. 1198-1201, 1988.
- [16] S. Kondo and R. Asai, “A reaction – diffusion wave on the skin of the marine angelfish pomacanthus”, Nature, 376, pp. 765-768, 1995.

- [17] H. Meinhardt, “Growth and patterning - dynamics of strip formation”, Nature, 376, pp. 722-723, 1995.
- [18] D. V. Petrov, “Splitting of an edge dislocation by an optical vortex”, Opt. & Quantum Electron., 34, pp. 759-773, 2002.
- [19] C. O. Weiss, M. Vaupel, K. Staliunas, G. Slekyš and V. B. Taranenko, “Solitons and vortices in lasers”, Appl. Phys. B: Lasers & Opt., B68, pp. 151-168, 1999.

簡歷

姓名： 寇人傑 (Ren-Jay Kou)

性別： 男

出生年月日： 民國 61 年 7 月 30 日

學歷： 國立中興大學物理系學士 [79.9-83.7]

國立交通大學光電工程研究所碩士 [83.9-85.7]

國立交通大學光電工程研究所博士 [85.9-92.7]

博士論文題目：

研究在大面積氧化侷限型之面射型雷射之橫向模態

Transverse Mode in Broad-Area Oxide-Confined Vertical-Cavity
Surface-Emitting Laser

Publication List

1. Ren-Jay Kou and Ci-Ling Pan, “Transverse Mode with Y-Junction Structures in Broad-Area Oxide-Confined Vertical-Cavity Surface-Emitting Laser”, *Jpn. J. Appl. Phys.*, 42, L458 (2003).
2. Ren-Jay Kou and Ci-Ling Pan, “Formation of the Transverse Mode with Y-Junction Structures in Broad-Area Oxide-Confined Vertical-Cavity Surface-Emitting Laser”, *Jpn. J. Appl. Phys.*, 42, L824 (2003).